

TABLE 2.1.

Dates for the Creation of the Universe Based on Biblical Chronology

Chronologist	Date for Creation of the Universe
Rabbi Jose ben Halafta	3760 BCE
Reverend John Lightfoot	3929 BCE
Christian Longomontanus	3964 BCE
Johannes Kepler	3993 BCE
Isaac Newton	3998 BCE
Bishop James Ussher	4004 BCE
Eusebius, Bishop of Caesarea	5203 BCE
Julius Africanus	5504 BCE



Figure 3.1. Zircon grains from Jack Hills, Western Australia. Each grain is a few tenths of a millimeter in length. Image courtesy of Aaron Cavosie, University of Puerto Rico, Mayagüez.

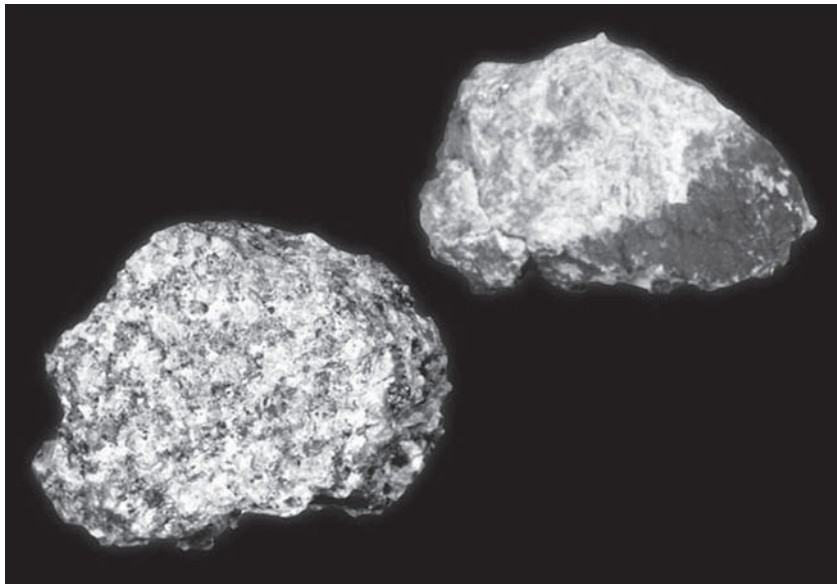


Figure 3.2. Ancient lunar crustal rocks collected on Apollo missions. These rocks are about 4.5 billion years old, indicating that parts of the Moon's crust solidified soon after the Moon was formed. Photo courtesy of NASA Johnson Space Center.

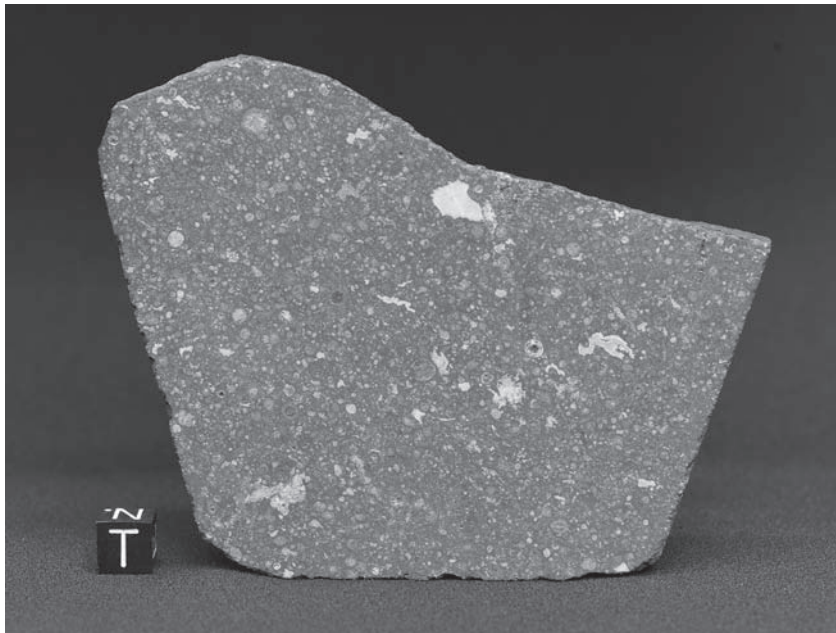


Figure 3.3. The Allende meteorite. The white to light gray, irregularly shaped speckles in the Allende meteorite are calcium-aluminum-rich inclusions (CAIs). Photo courtesy of Laurence Garvie/ASU; courtesy of Center for Meteorite Studies, ASU.

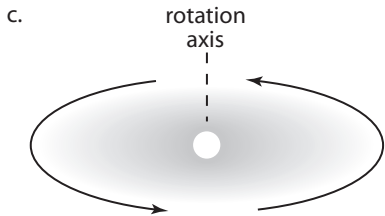
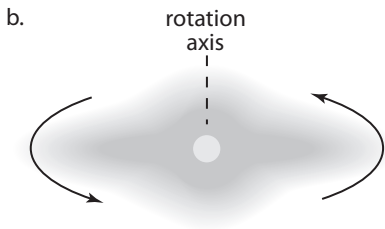
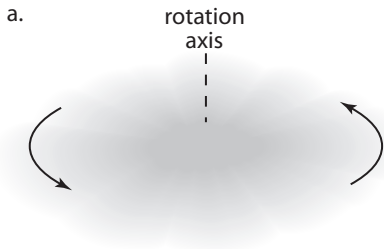


Figure 4.1. Illustration of the theory that stars form from rotating clouds of gas in space.

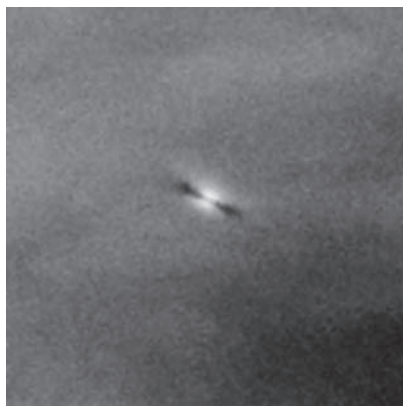


Figure 4.2. Hubble Space Telescope images showing flattened disks around newborn stars (known as *proplyds*) in the Orion Nebula. Image courtesy of NASA, ESA and L. Ricci (ESO).

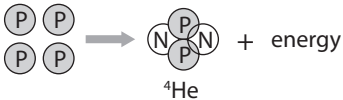


Figure 4.3. In the proton-proton chain, four protons combine to form a helium nucleus. In the process, some mass is converted into energy and a small amount of mass is converted into particles called neutrinos. This nuclear fusion reaction generates the energy that powers the Sun.

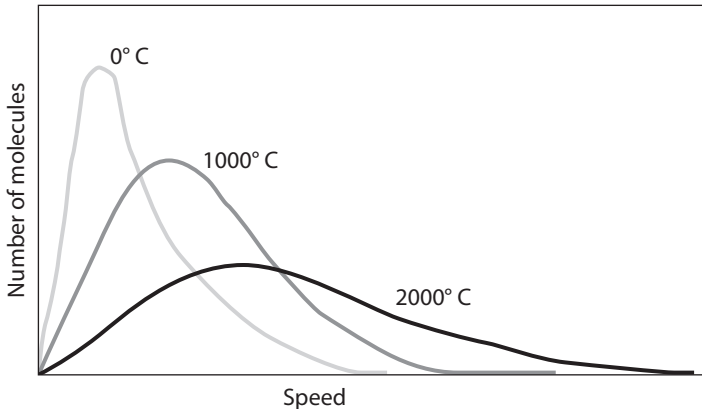


Figure 4.4. The Maxwell-Boltzmann distribution depicts the speed (x value) versus the number of particles in a gas moving at each speed (y value). As the gas temperature increases, the entire distribution broadens and shifts toward higher speeds. In the core of the Sun, only a very few particles with the very highest speeds have enough energy to participate in nuclear fusion reactions.



Figure 5.1. The Big Dipper. Some stars appear brighter than others; however, the brightest stars may not be intrinsically brighter than the fainter stars. Instead, they may be intrinsically faint stars that happen to be near the Sun. Image courtesy of Noel Carboni.

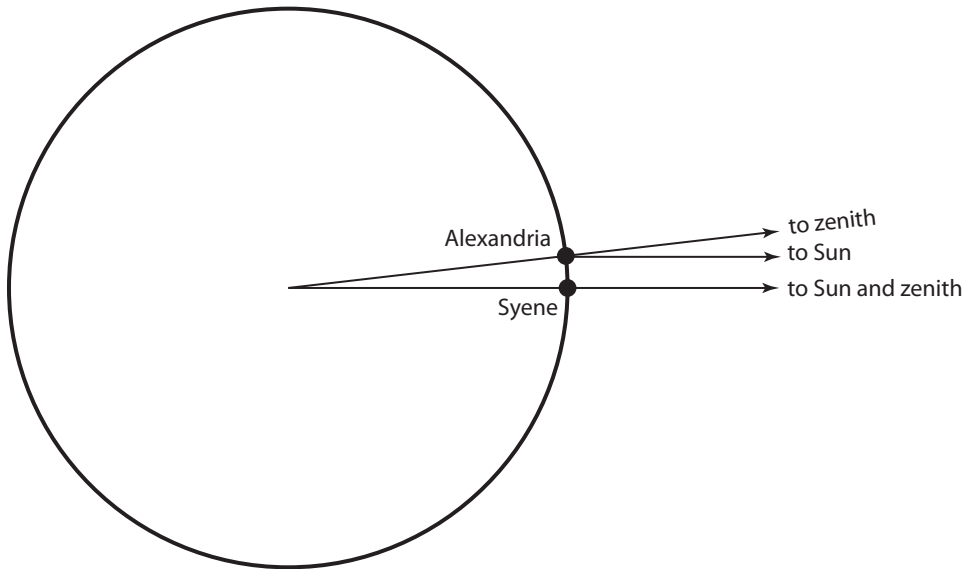


Figure 5.2. Eratosthenes' method for measuring the circumference and diameter of the Earth.

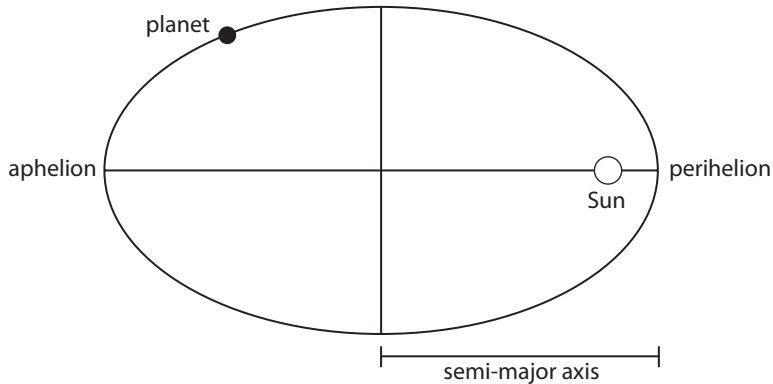


Figure 5.3. Kepler discovered that planets orbit the Sun in ellipses, not circles. The size of an orbit is typically described in terms of the semi-major axis of the ellipse (half the length of the long axis). For the Earth's orbit, this length is one astronomical unit. The closest approach of the planet to the Sun is called the *perihelion point*, the point at which the planet is furthest from the sun is the *aphelion point*.

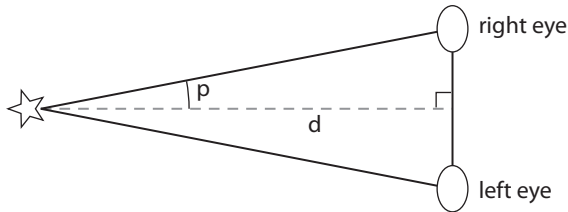


Figure 5.4. Parallax is the perceived change in direction or position of an object when we view that object from two different locations. We do this all the time using our binocular vision (as each of our eyes is at a slightly different viewing location).

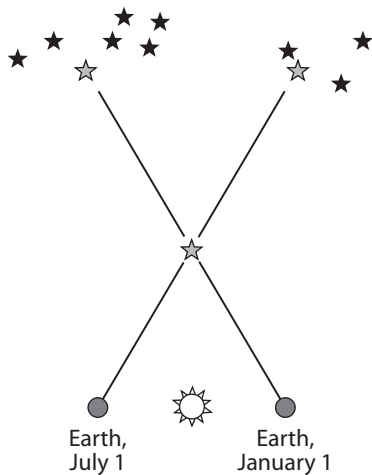


Figure 5.5. Annual parallactic motion. Between January and July, the Earth has moved halfway around its orbit. When we view a nearby star in January and again in July, that star will appear to have moved relative to the positions of more distant stars.

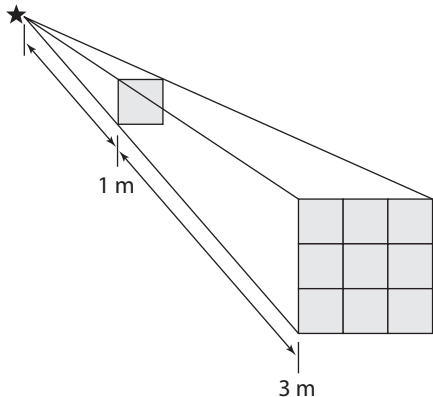


Figure 6.1. The inverse square law. When an object is at a distance of three meters from a light source, the light source must illuminate nine times more area than if the same object were at a distance of one meter. As a result, the light on each square is one-ninth as bright at a distance of three meters as at a distance of one meter.

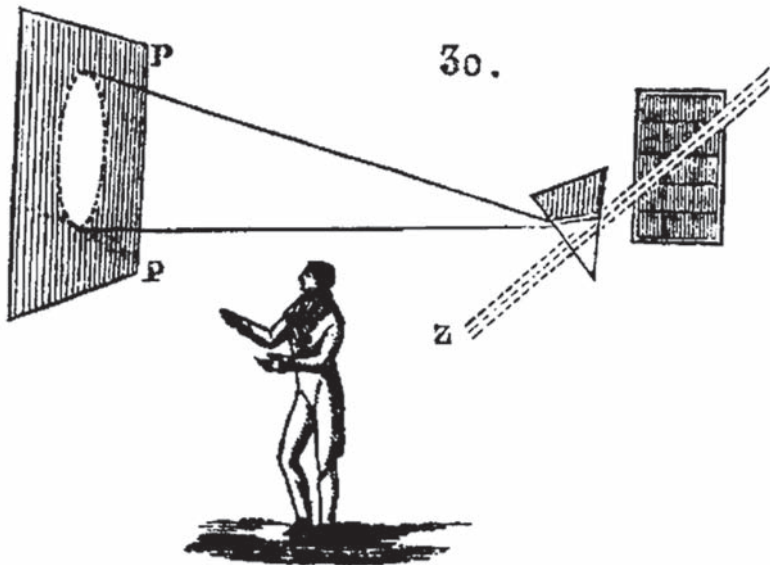


Figure 7.1. Newton's experiment with white light, in which he demonstrated that white light from the Sun can be dispersed into a rainbow of colors, as presented in a sketch redrawn from Voltaire's *Eléments de la Philosophie de Newton*, published in 1738.

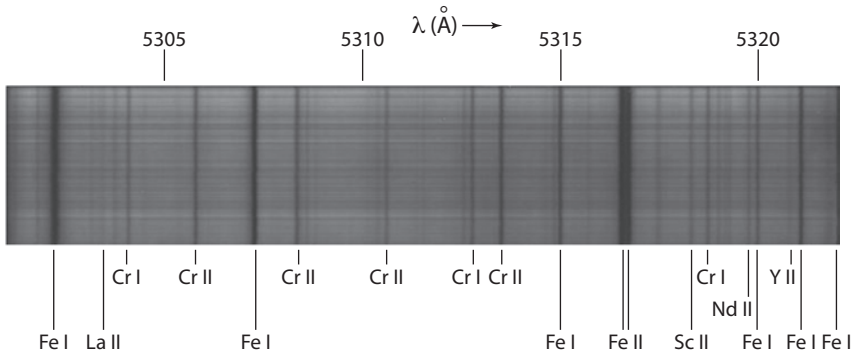


Figure 7.2. A modern spectrum showing the kinds of dark lines originally seen by Fraunhofer and Wollaston in the early nineteenth century. The labels at the top indicate the wavelength of light (in units of angstroms; one angstrom is one ten-billionth of a meter), the labels at the bottom which elements are responsible for which lines. Image courtesy of E. C. Olson, Mount Wilson Observatory.

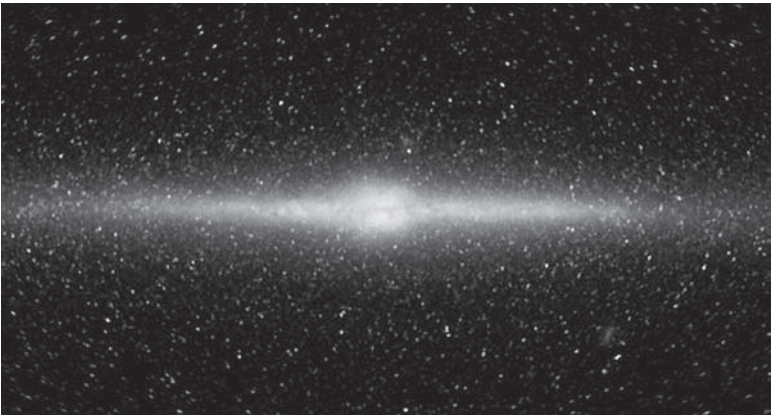
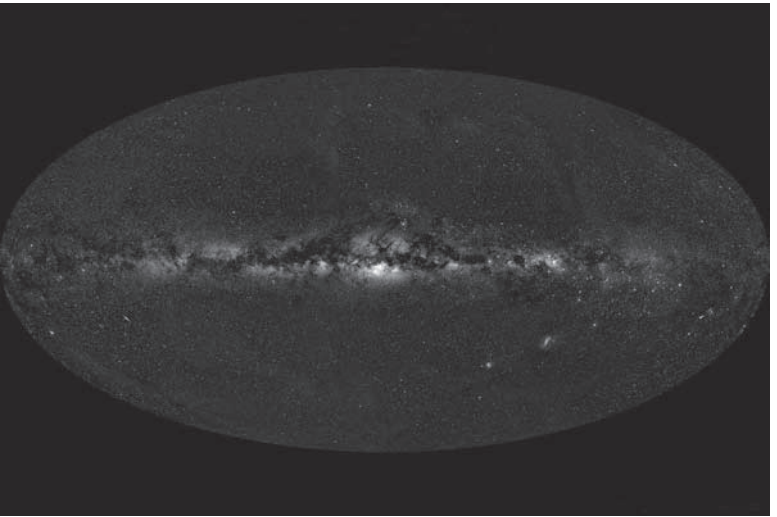


Figure 7.3. Top, the Milky Way seen in visible light. There are very bright regions due to the accumulated light from millions of stars, as well as numerous patches of darkness where dusty, interstellar clouds block the light of the stars. Bottom, the Milky Way as seen in infrared light. The overall bright glow is produced mainly by heated clouds of interstellar dust. Images courtesy of Axel Mellinger (top), E. L. Wright, The COBE Project, DIRBE, and NASA (bottom).

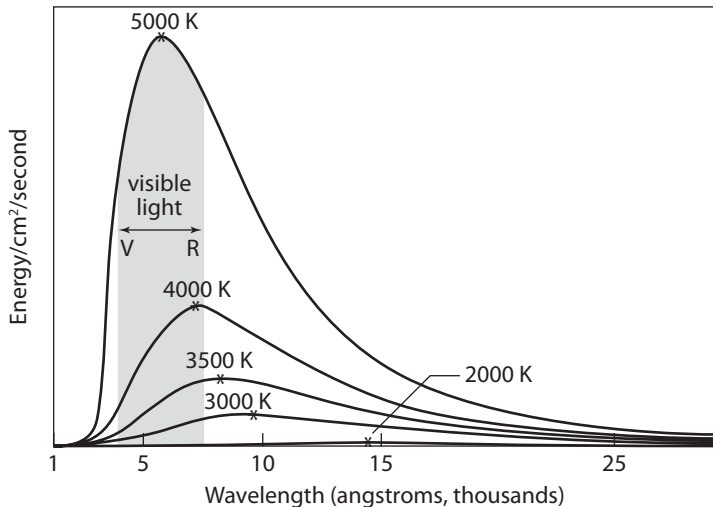


Figure 7.4. Blackbodies of different temperatures. Objects known as blackbodies emit energy in the form of light at all wavelengths, from gamma and X-rays (left) to radio waves (right). At a given temperature, a blackbody emits more energy per second at one wavelength than any other wavelength. The wavelength at which a blackbody emits the most energy depends only on the temperature of the blackbody. This illustration shows blackbody curves for blackbodies at temperatures of 5,000 K (close to the temperature of the Sun; most of the light is emitted as visible light), 4,000 K, 3,500 K, 3,000 K, and 2,000 K (most of the light emitted is infrared).

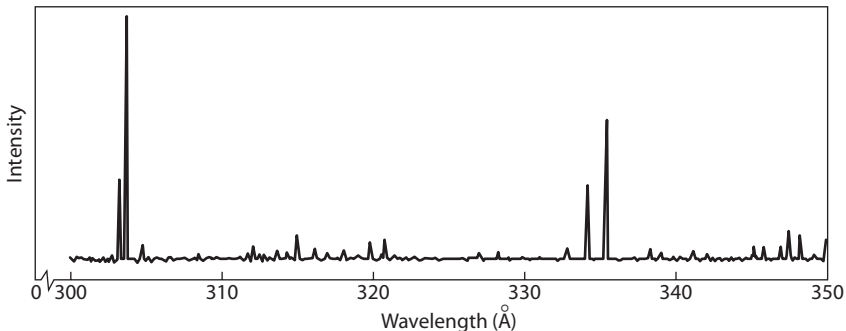


Figure 8.1. Two views of an ultraviolet spectrum of the Sun. Top, the photographic image of the spectrum, revealing the bright lines that mark wavelengths at which ultraviolet light, between the wavelengths of 300 and 350 angstroms, emerges from the Sun. Bottom, a plot of the intensity or brightness of the spectrum across the same wavelength range. Image courtesy of NASA.

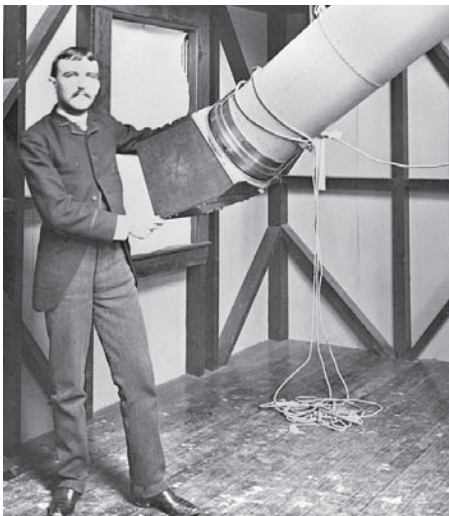


Figure 8.2. Left, undated photograph of Henry Draper. Right, undated photograph of Draper at his telescope. Left image courtesy of the Draper Family Collection, Archives Center, National Museum of American History, Smithsonian Institution; right image courtesy of the Photographic History Collection, Division of Information Technology and Communications, National Museum of American History, Smithsonian Institution.



Figure 8.3. Left, Edward Pickering. Right, room full of women “computers” at Harvard College Observatory, 1892. Fleming is seen standing in the middle of the group. Images courtesy of Harvard College Observatory photo collection.



Figure 8.4. Left, Annie Jump Cannon in her Oxford robe in 1925. Right, Cannon at work classifying spectra. Images courtesy of Harvard College Observatory photo collection.

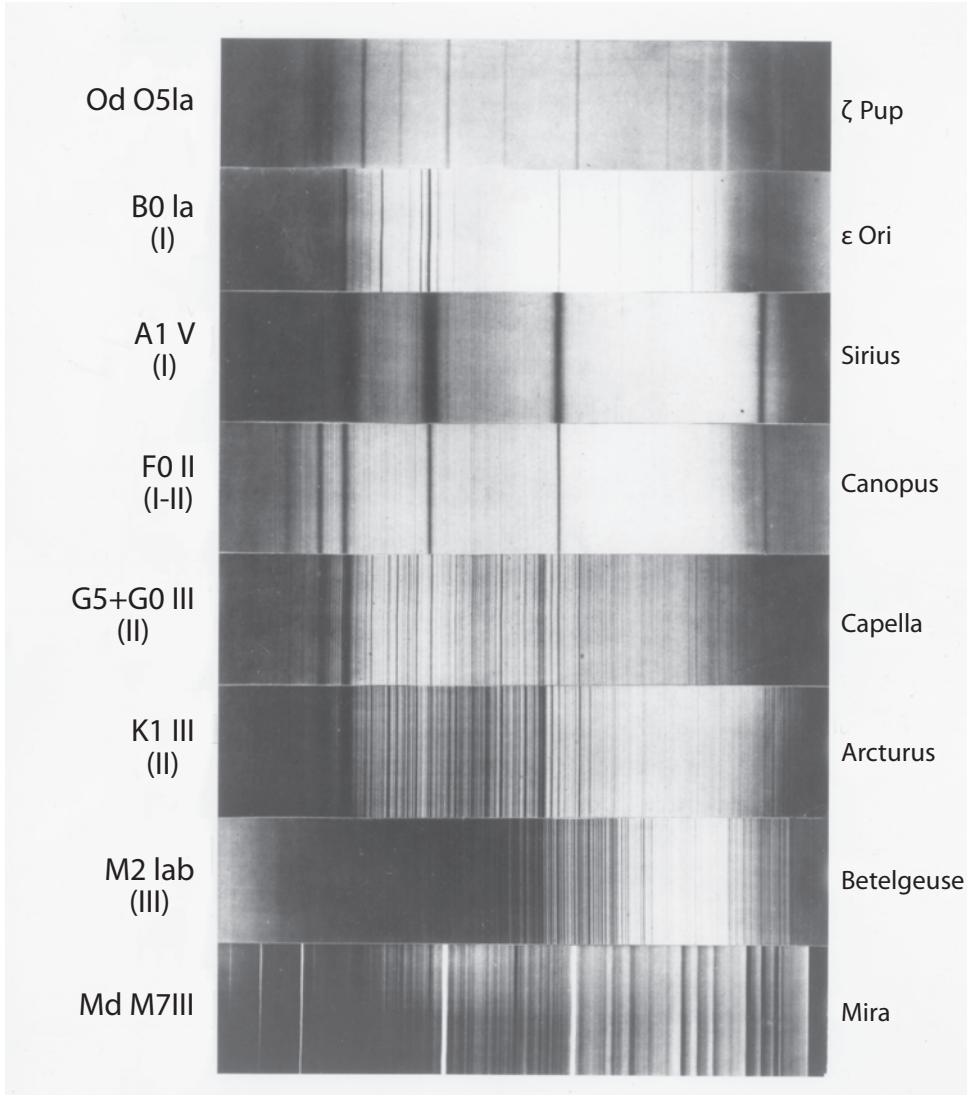


Figure 8.5. The classic spectral sequence as seen in photographic spectra of an O5 star (Zeta Puppis), a BO star (Epsilon Orionis), an A1 Star (Sirius), an FO star (Canopus), a G2 star (Capella), a K1 star (Arcturus), an M2 star (Betelgeuse), and an M7 star (Mira). The strong (dark) lines in these negative images for Sirius are due to hydrogen. The signature of hydrogen is weaker going both upwards and downwards in the spectral sequence. The strong lines in the O5 star are due to ionized helium, in the BO star to neutral helium. The strong lines on the left side of the F, G, and K spectra signal calcium, and the absorption bands in the M7 spectrum indicate the molecule titanium oxide. Image courtesy of Jim Kaler.



Figure 8.6. Left, Ejnar Hertzsprung. Right, Henry Norris Russell. Images courtesy of Yale University Library (left) and the AIP Emilio Segre Visual Archives, W. F. Meggers Collection.

OBSERVED PARALLAXES.

No.	Star	R.A. 1900	Decl. 1900	Mag.	Sp.	P.M.	Parallax	p. e.	Pl.	Comp Star	Observed p. e.	Absolute Magnitude	Cross Vel'y Km/Sec
1	β Cassiopeiae	0 3.8	+58 36	2.42	F_5	0.56	+0.082	± 0.019	5	9	± 0.009	2.1	31
2	Groombr. 34	0 12.7	+43 27	7.73	Ma	2.80	+0.250	± 0.016	6	9	± 0.011	9.8	51
3	26 Andromedae	0 13.3	+43 15	6.04	A	0.03	-0.026	± 0.042	6	9	± 0.041
4	η Cassiopeiae	0 43.0	+57 17	3.64	F_8	1.24	+0.187	± 0.019	7	8	± 0.021	5.1	30
5	α Ceti	2 14.3	- 3 26	var.	Md	0.24	+0.136	± 0.035	7	9	± 0.035	2.5 to 10.4	8
6	ρ Persei	2 58.8	+38 27	var.	Mb	0.17	+0.083	± 0.040	7	9	± 0.040	3.1 to 3.9	9
7	β Persei	3 1.7	+40 34	var.	B_8	0.01	+0.007	± 0.027	7	8	± 0.025
8	Lal. 6888 }	3 40.2	+41 9	8.35	G	1.38	-0.029	± 0.033	6	6	± 0.033
9	Lal. 6889 }			8.89			+0.020	± 0.034			± 0.035

Figure 8.7. First nine lines of a table from Henry Norris Russell's 1910 paper, showing measured values of parallax for stars (Column 8), which he used with the measured apparent magnitudes of these stars (column 5) to calculate absolute magnitudes (column 13). With these absolute magnitudes, Russell had incontrovertible evidence that some stars of a given spectral type are faint (star 4), while others of the same spectral type (star 1) are bright.

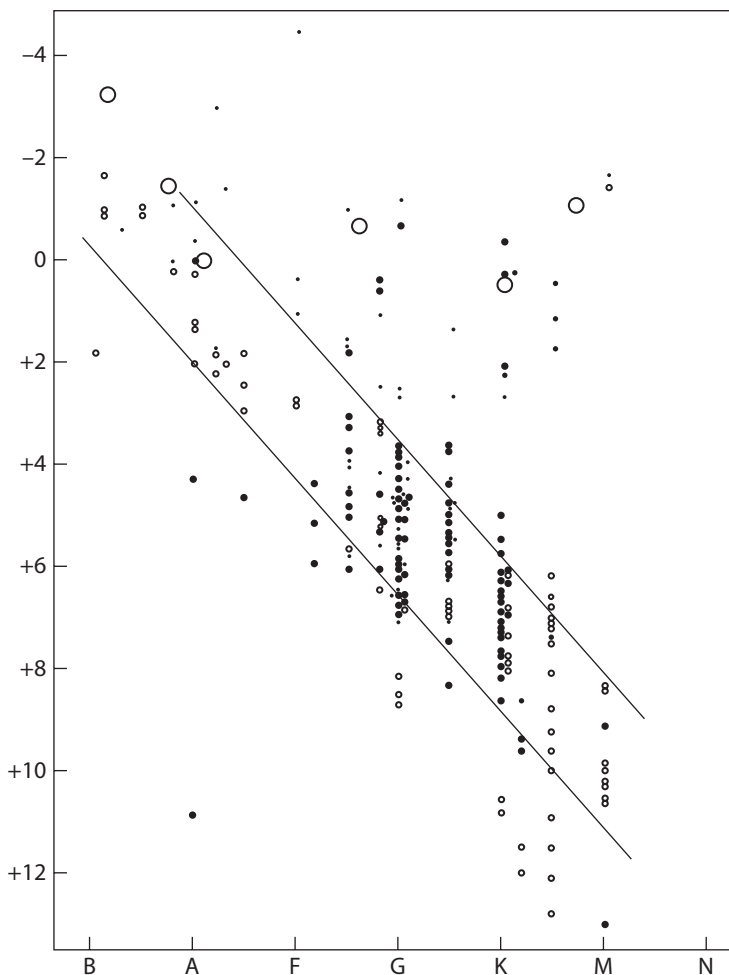


Figure 8.8. The first Hertzsprung-Russell (H-R) diagram, published in 1914 by Henry Norris Russell (*Nature* 93: 252). The horizontal axis indicated spectral type (a proxy for temperature), with the hottest stars at the left, the coolest at the right. The vertical axis shows absolute magnitude, with the brightest stars at the top, the faintest at the bottom. The small solid and open dots represent measurements of individual stars; the large open circles are average measurements for groups of stars (the six open circles include data for 120 stars). The diagram shows the absence of faint white stars (lower left) and shows that the faintest stars are red (lower right). Red stars can however be either faint or extremely bright (top right). Russell noted that although there is some scatter both above and below, most stars cluster between the two diagonal lines in the region that has come to be known as the *main sequence*.

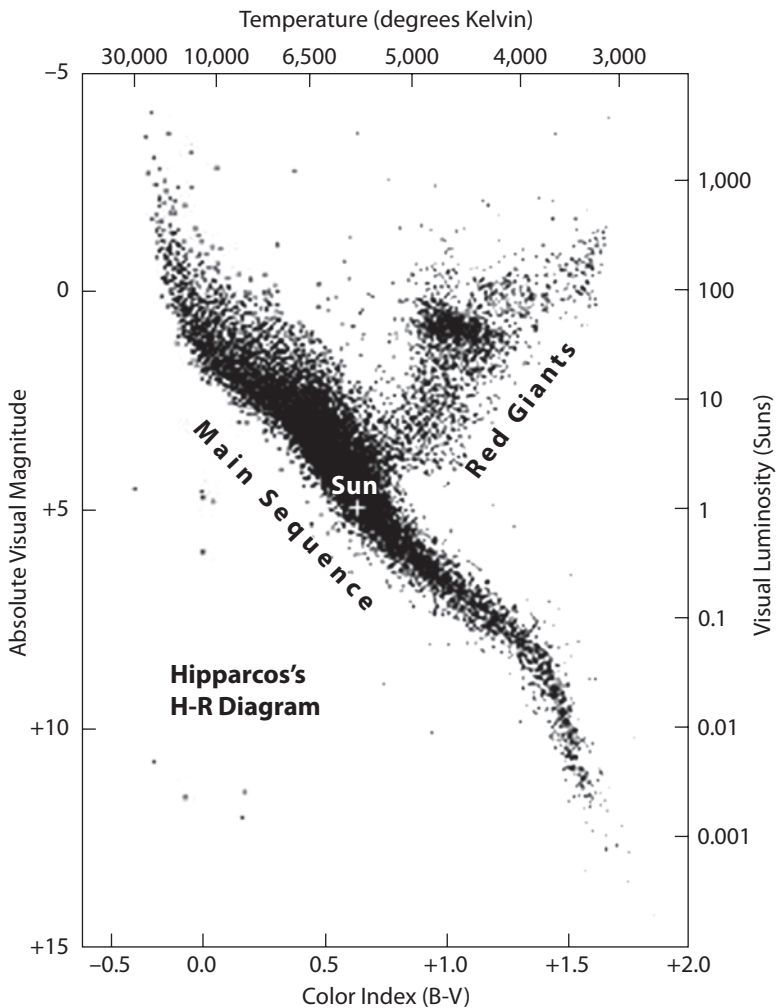


Figure 9.1. H-R diagram made from 20,853 stars observed by the Hipparcos satellite. The temperature (equivalent to spectral type) is marked along the horizontal axis at the top of the plot. The surface temperature of a star can also be estimated fairly accurately by measuring the intensity (or magnitude) of light from the star in two different broadband filters (for example, U for ultraviolet, B for blue, V for visible, R for red) and calculating the difference between these two magnitudes. Astronomers call this difference a *color* or *color index* (e.g., the B-V color; say “B minus V color”). A star with a large B-V color is very red and cool; one with a negative B-V color is very blue and hot. This color (marked along the bottom of the plot) is unique for each temperature across the broad range of temperatures that characterize stars. Thus, the horizontal axis of an H-R diagram could be plotted as a function of spectral type, temperature, or color. The brightnesses of the stars are plotted along the vertical axis, either in terms of the absolute magnitude (left) or in comparison with the luminosity of the Sun (right). Image courtesy of Michael Perryman.

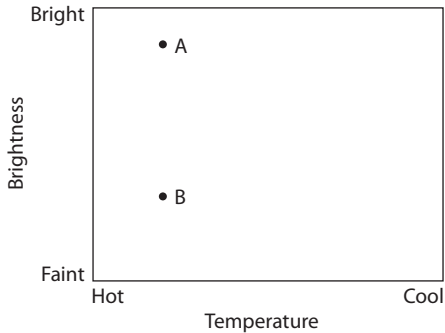


Figure 9.2. A comparison of two stars, A and B, on an H-R diagram. Stars A and B have the same temperature, but Star A is much brighter than Star B. Therefore, Star A must be much larger (with more surface area from which to emit light) than Star B.

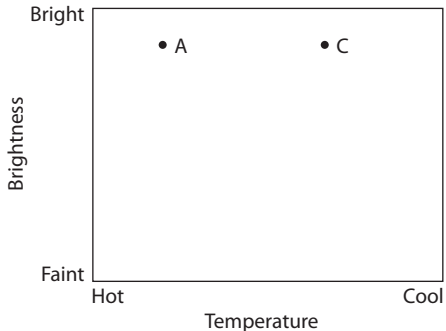


Figure 9.3. A comparison of two stars, A and C, on an H-R diagram. Stars A and C emit the same total amount of light, but Star A is much hotter than Star C and consequently emits much more light from every square meter of its surface than Star C. Therefore, Star C must be larger (with more surface area from which to emit light) than Star A in order to compensate for emitting light less effectively.

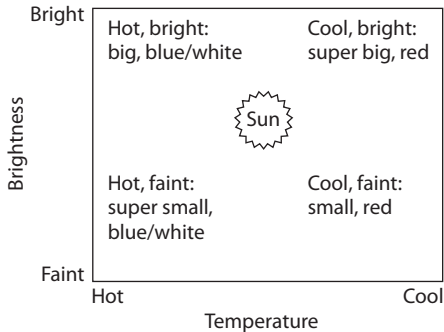


Figure 9.4. A comparison to the Sun of the relative properties of stars in the four corners of the H-R diagram.

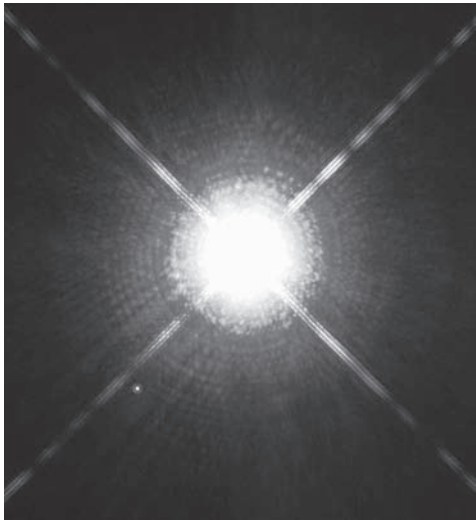


Figure 9.5. Sirius (center) and Sirius B (toward lower left corner). Image courtesy of the Space Telescope Science Institute.

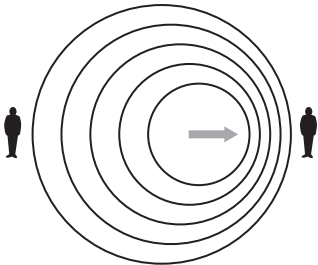


Figure 10.1. Illustration of Doppler shift, with light source moving to the right.

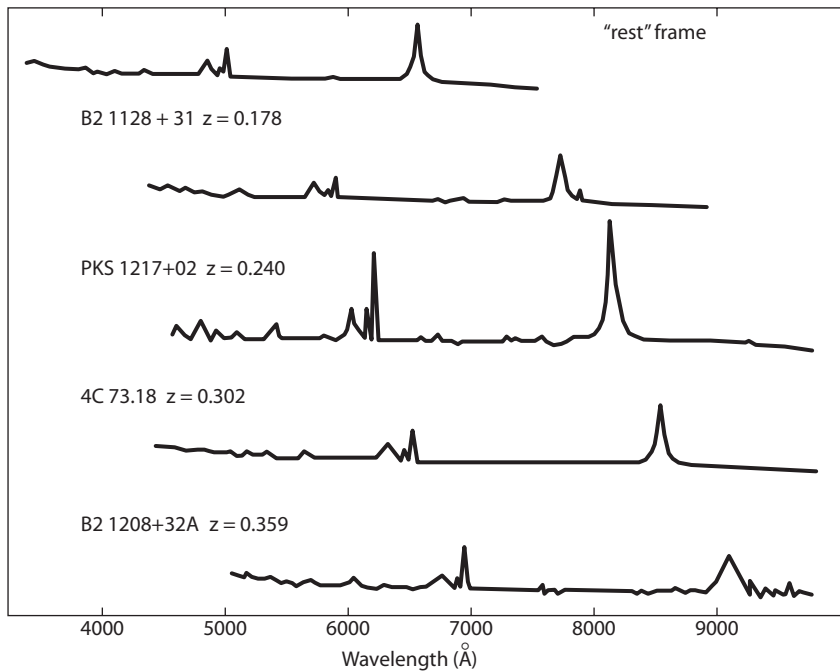


Figure 10.2. A spectrogram recorded by a Kitt Peak National Observatory telescope, in which the top spectrum (obtained for a hydrogen light source at rest in the laboratory) has peaks for three hydrogen lines in the blue (4,340 angstroms), green (4,861 angstroms), and red (6,563 angstroms). The bottom four spectra are from distant quasars at progressively greater distances and show the hydrogen lines shifted ever greater distances toward the right (red) end of the spectrum. Image by M. Corbin.

TABLE 10.1.

Stellar Masses: Russell Breaks the Code

Spectral Type	Average Stellar Mass
B	$17 M_{\text{sun}}$
A	$5 M_{\text{sun}}$
F	$3.5 M_{\text{sun}}$
K and M	$< 1 M_{\text{sun}}$

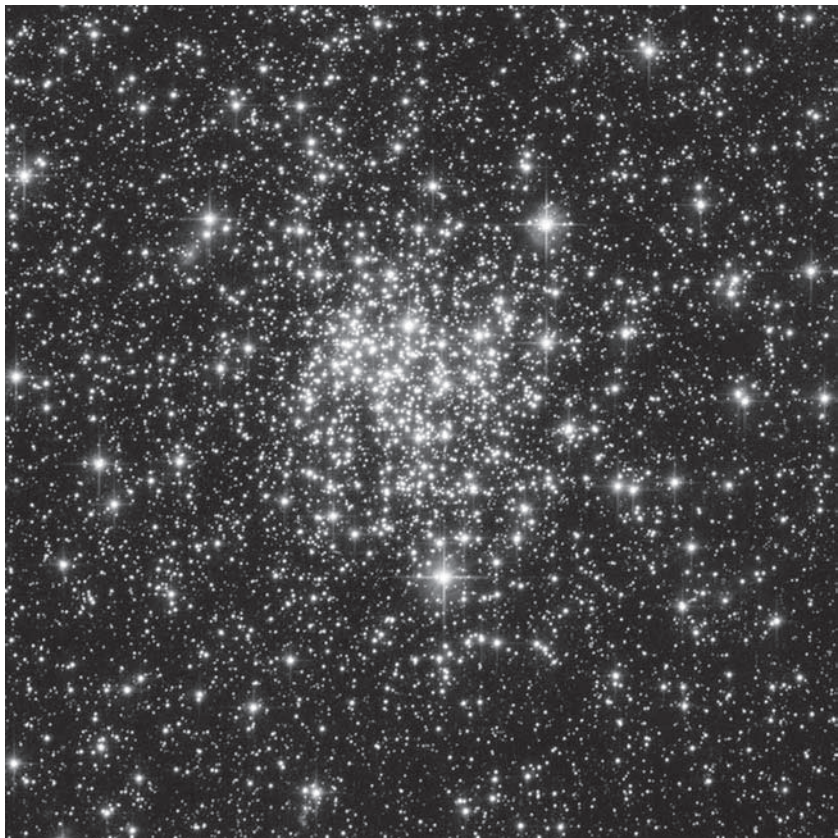


Figure 11.1. The open cluster NGC 265, located in the Small Magellanic Cloud. Image courtesy of E. Olszewski, University of Arizona, the European Space Agency and NASA.

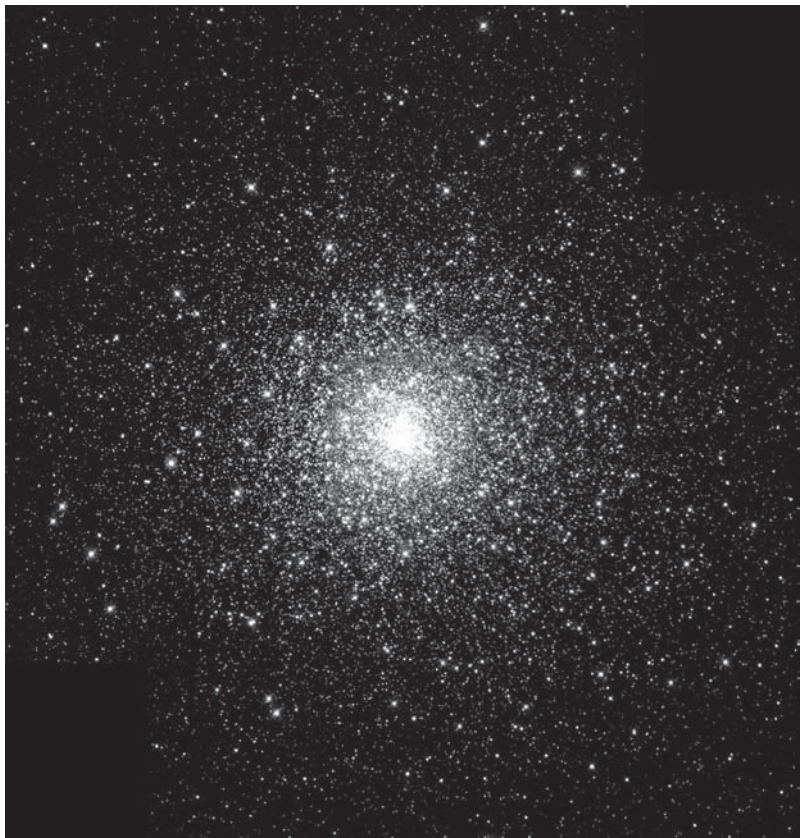


Figure 11.2. The globular cluster M80, located in the Milky Way. Image courtesy of the Hubble Heritage team (AURA/STScI/NASA).



Figure 11.3. The scattered group of stars in the central part of the image is the open star cluster called the Hyades in the constellation of Taurus. The Hyades can be seen easily by the naked eye as a “V” shape in the sky. The brightest star, Aldebaran, which represents the red eye of Taurus the bull, does not physically belong to the cluster. Image courtesy of Till Credner, AlltheSky.com.

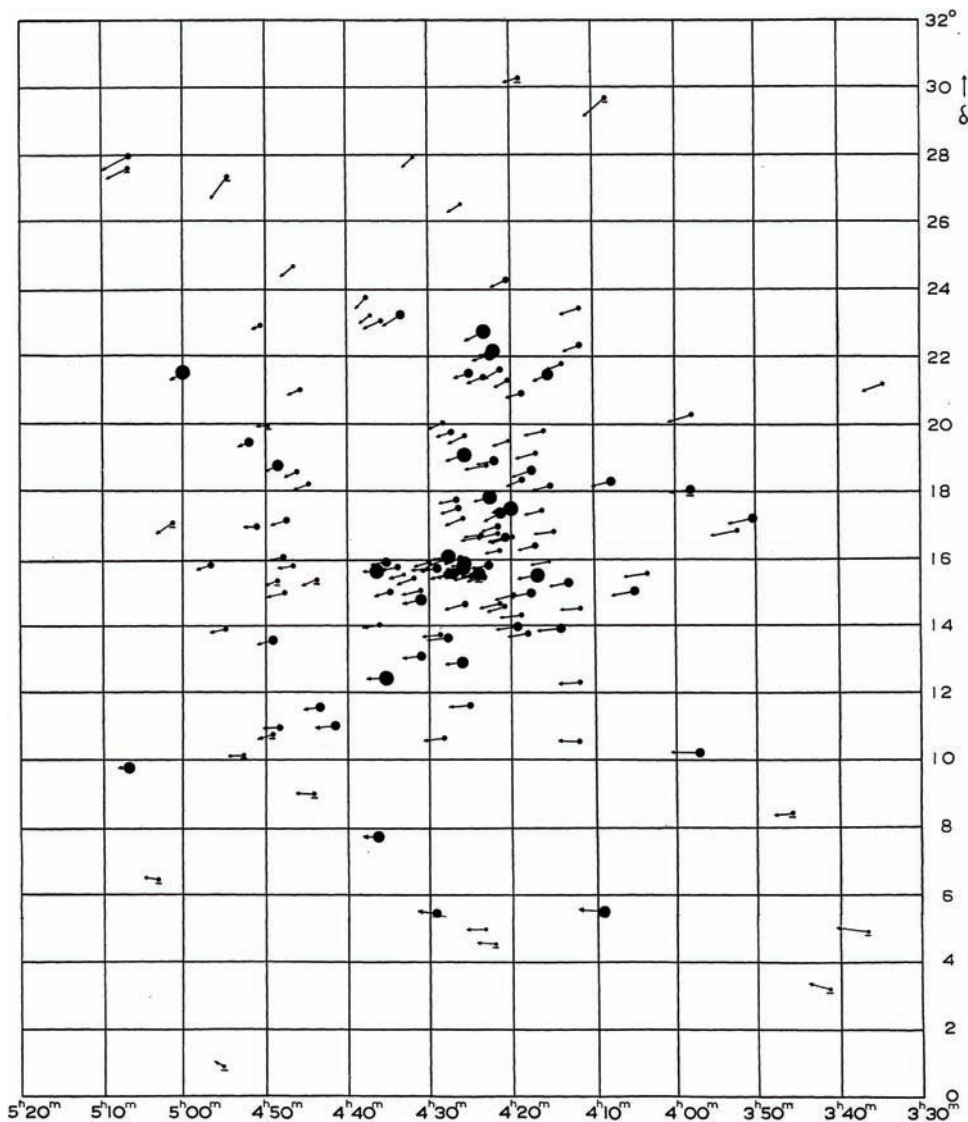


Figure 11.4. The directional (proper) motions of the stars in the Hyades Cluster, depicted with arrows indicating the direction in which each star is moving. The stars appear all to be moving toward a single “convergent” point, located to the left of the left edge of the graph. From H.G. van Bueren, *Bulletin of the Astronomical Institutes of the Netherlands* 11 (May 1952): 385.

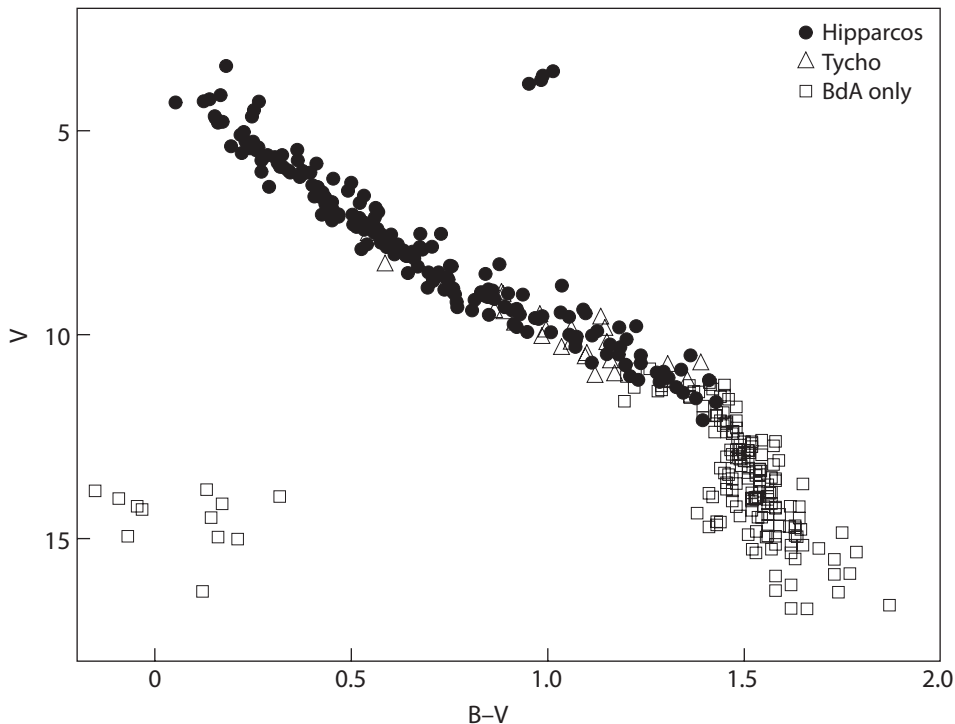
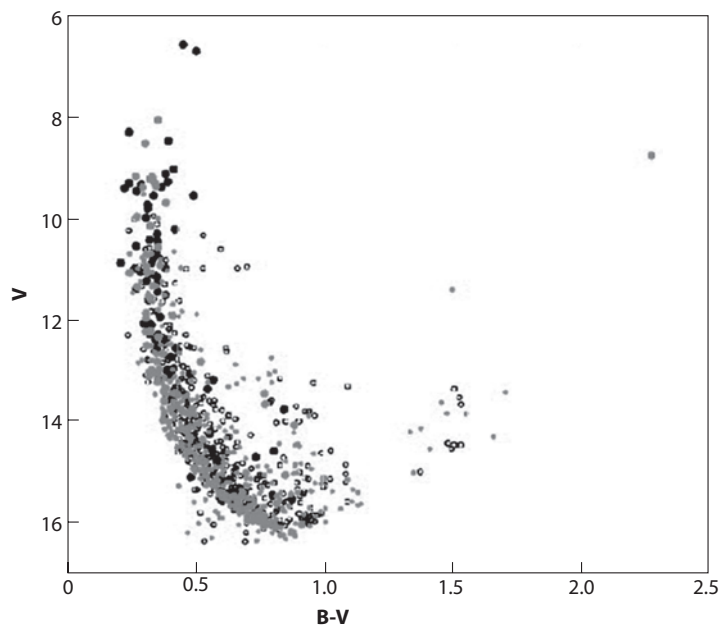
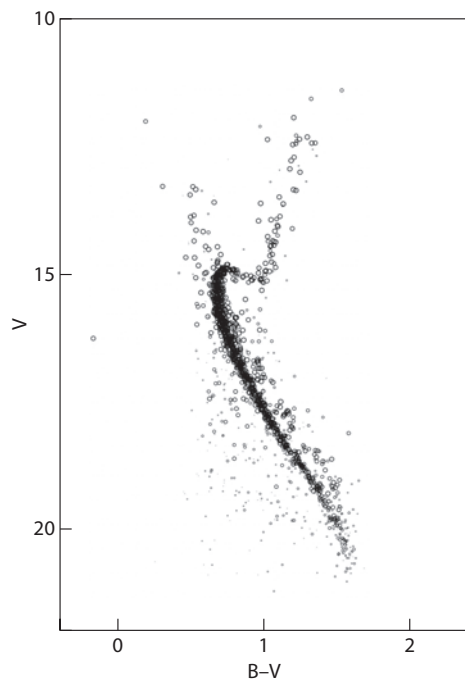
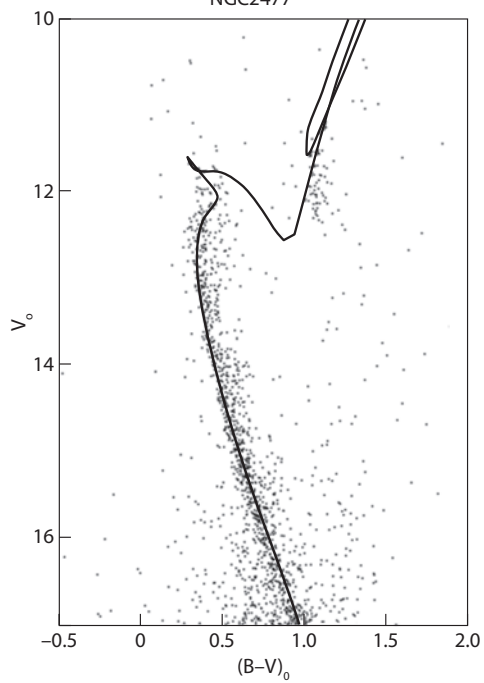


Figure 11.5. H-R diagram for the Hyades Cluster, plotting the absolute magnitude in the V (visual) band versus the B-V color. (Versions of H-R diagrams that use B-V color instead of spectral type are known as color-magnitude diagrams. Color-magnitude diagrams plot actual observed quantities while H-R diagrams plot quantities [temperatures] calculated from the observed colors or spectra for the stars.) The diagram shows the main sequence for the Hyades, along with some red giants (top right) and white dwarfs (bottom left). From Perryman et al., *Astronomy & Astrophysics* (1998) 331, 90. Reproduced with permission © ESO.

NGC2477



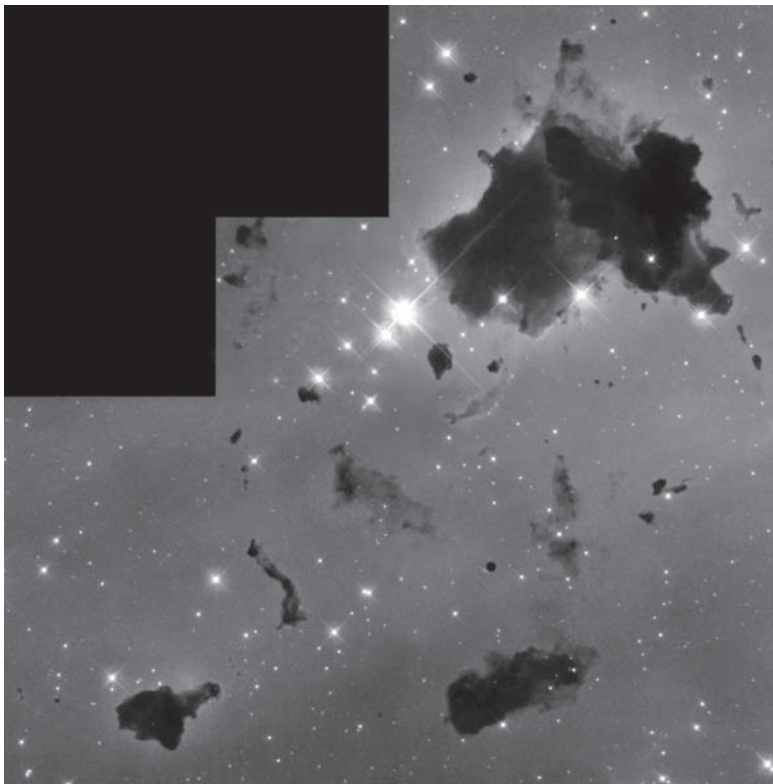


Figure 12.1. Thackeray's globules are dense, opaque clouds of gas and dust in which stars may be forming. These globules are seen silhouetted against nearby, bright, newborn stars in the star-forming region known as IC 2944. Image courtesy of Bo Reipurth (University of Hawaii), NASA, and the Hubble Heritage team (STScI/AURA).



Figure 12.2. Star birth clouds in M16. The stars are embedded inside finger-like protrusions extending from the top of the nebula. Each “fingertip” is somewhat larger than our solar system. Image courtesy of NASA, ESA, STScI, and J. Hester and P. Scowen (Arizona State University).

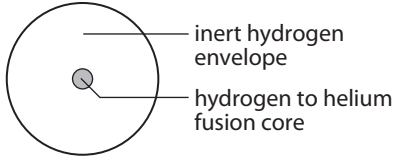


Figure 13.1. The internal structure of a star when it is on the main sequence. In the core, hydrogen fuses to helium. An inert hydrogen envelope surrounds the core. The diameter of the core is about 10 percent of the diameter of the star.

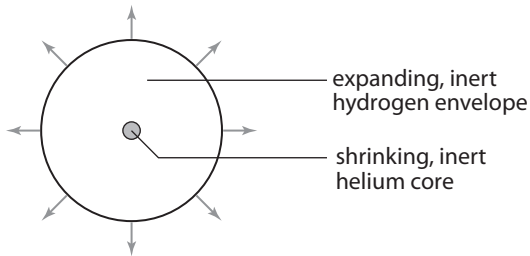


Figure 13.2. The internal structure of a star when it leaves the main sequence. In the core, the hydrogen fuel is exhausted and the helium is too cool for fusion. The cooling core contracts, which has the effect of heating the surrounding hydrogen envelope, causing the outer layers of the star to expand. The star is now a subgiant.

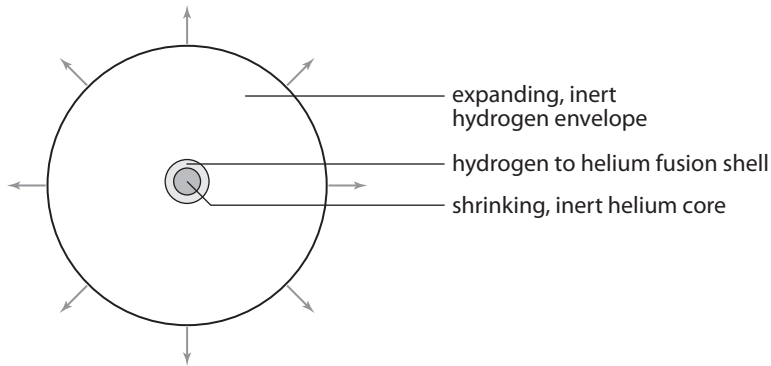


Figure 13.3. The internal structure of a star when it climbs the red giant branch. The helium core continues to contract. Surrounding that core, a shell of hydrogen becomes hot enough to fuse into helium. The release of heat from the fusion reactions further heats the outer hydrogen envelope, causing it to expand even more. The star is now a red giant.

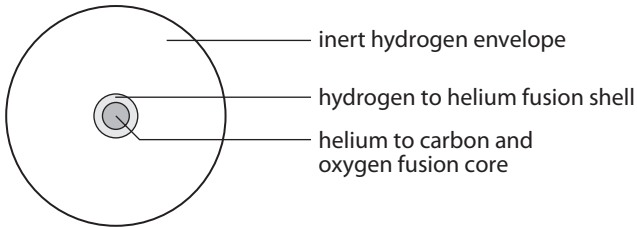


Figure 13.4. The internal structure of a star in which the core has become hot enough for the helium to fuse into carbon and oxygen. The star is now a horizontal branch star.

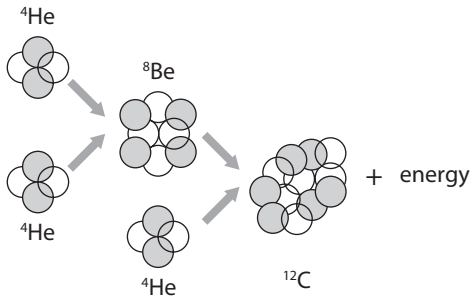


Figure 13.5. The triple-alpha process for nuclear fusion. Three helium nuclei combine, through a series of collisions, to form a single carbon nucleus and release energy as gamma rays.

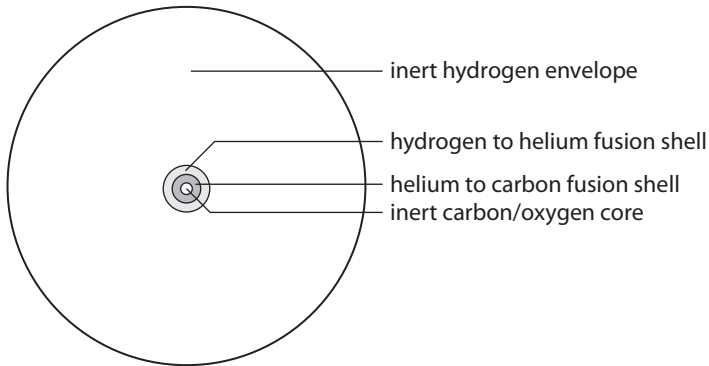


Figure 13.6. The internal structure of a red supergiant star. At the center, an inert core of carbon and oxygen is being deposited as the residue of the fusion of He. This core will be left behind as a white dwarf, after the star expels its outer layers in the planetary nebula phase.

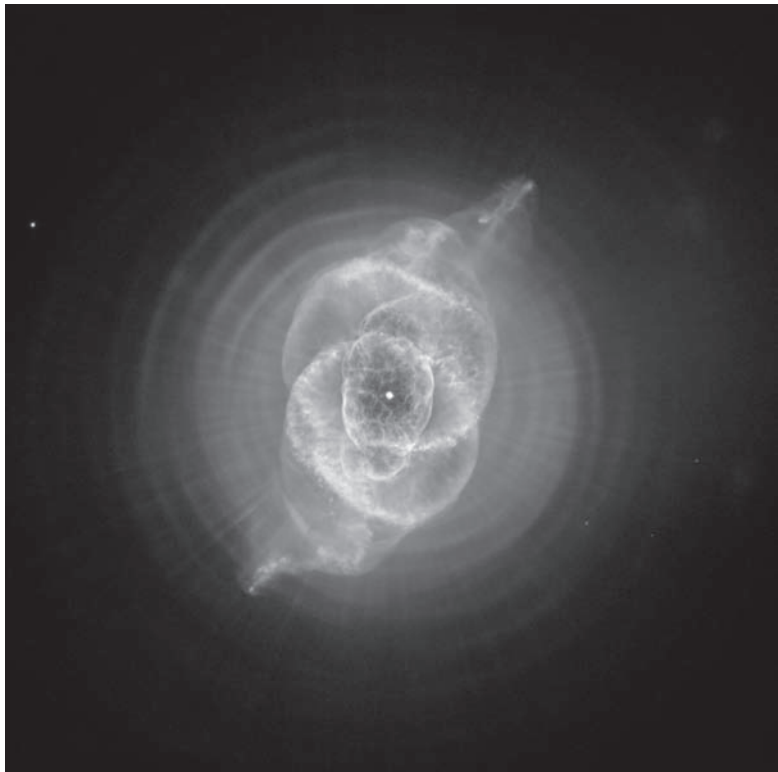


Figure 13.7. Hubble Space Telescope image of the Cat's Eye Planetary Nebula. Image courtesy of NASA, ESA, HEIC, and the Hubble Heritage team (STScI/AURA).

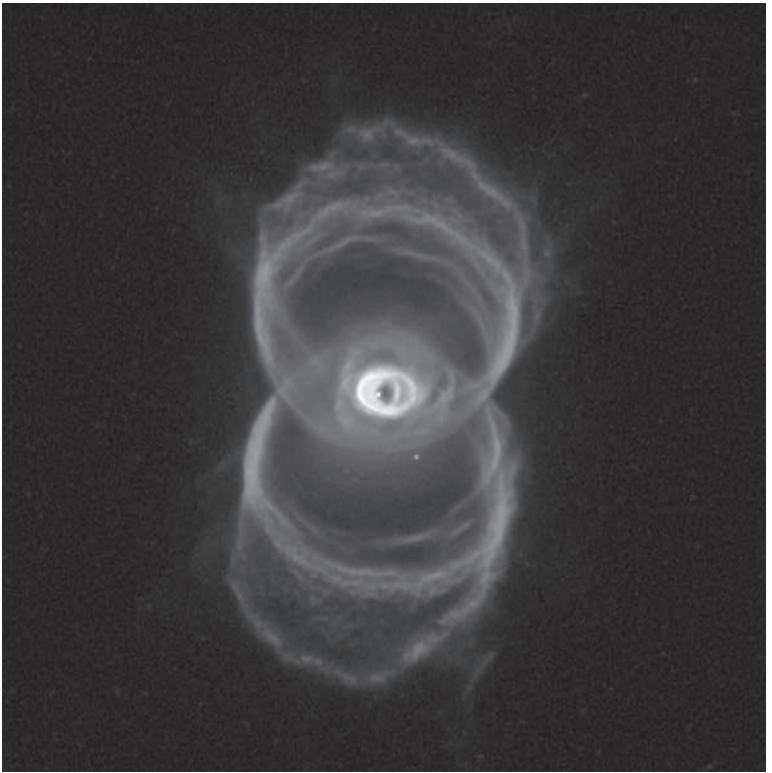


Figure 13.8. Hubble Space Telescope image of the Hourglass Planetary Nebula. Image courtesy of Raghvendra Sahai and John Trauger (JPL), the WFPC2 science team, and NASA.

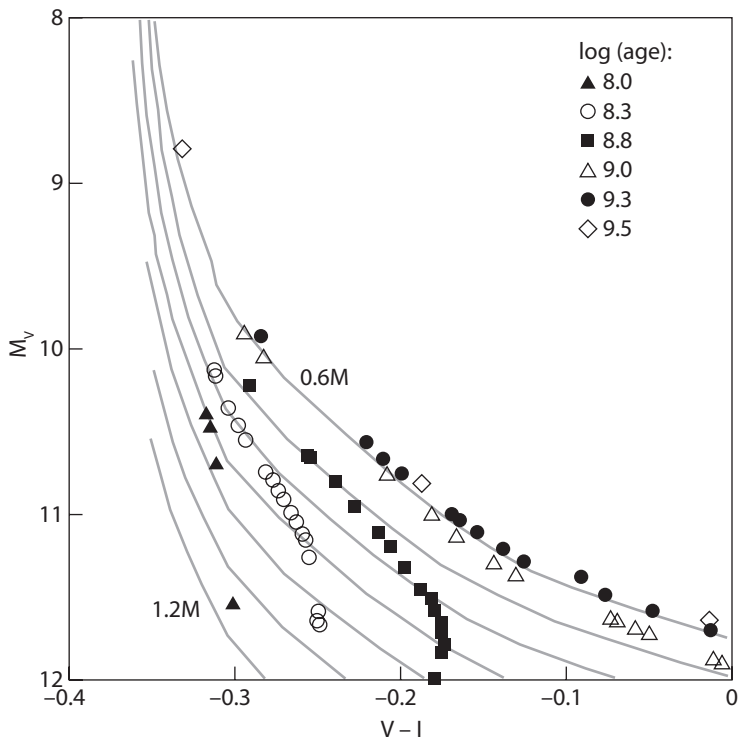


Figure 13.9. Cooling curves for white dwarfs on a color-magnitude diagram. This plot shows only the white dwarf section of the diagram. The lines show the cooling curves for white dwarfs with masses ranging from 0.6 solar masses (top curve) to 1.2 solar masses (bottom curve). White dwarfs with different radii (i.e., masses) can have the same temperature (i.e., $V-I$ color) and thus will have different luminosities. Note that, counterintuitively, more massive white dwarfs are smaller and therefore less luminous than less massive white dwarfs. Any single white dwarf has a fixed mass and will slide down a cooling curve as it ages, becoming fainter (larger in absolute magnitude) and cooler (with less negative $V-I$ color). Any single star cluster of a given age (see symbols) would have white dwarfs representing a range of masses. From Jeffrey et al., *The Astrophysical Journal* (2007): 658, 391.

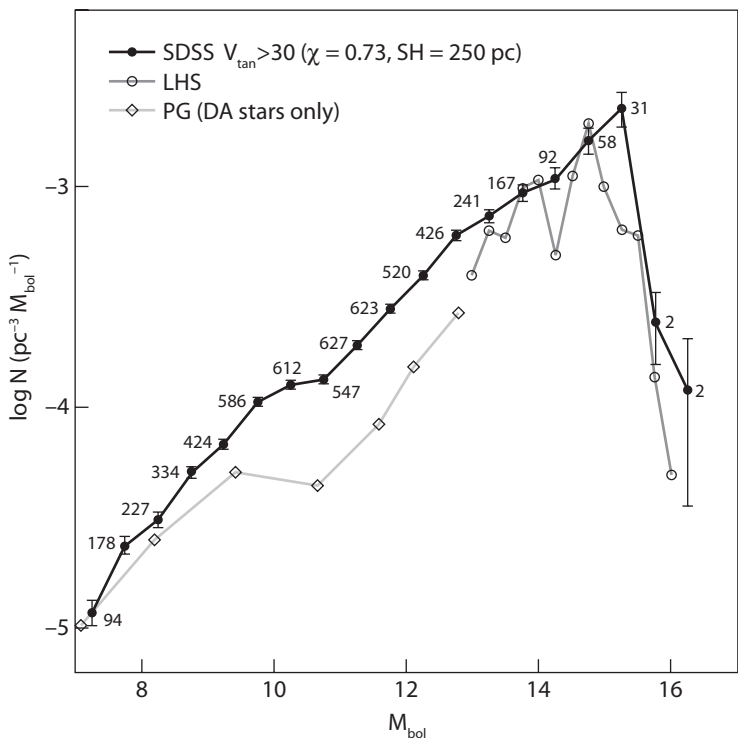


Figure 13.10. This plot shows the number of known white dwarfs per volume segment of the galaxy at different brightnesses (y-axis) plotted as a function of their brightness (x-axis) observed as part of the Sloan Digital Sky Survey. The dashed and dotted lines indicate white-dwarf measurements from other observing projects. Brightness is measured in units of *bolometric magnitude* (or M_{bol}), which indicates the total amount of energy emitted by the white dwarf at all wavelengths, from X-rays to radio waves. The faintest stars are to the right, the brightest to the left. The number of white dwarfs is measured as stars per cubic parsec at each bolometric magnitude. On the plot, the numbers indicate the total number of white dwarfs observed that contribute to each data point. For example, these data indicate that 586 white dwarfs are known with $M_{\text{bol}} = 10$. The volume of the galaxy surveyed by the SDSS to find these white dwarfs indicates the presence of about one white dwarf of this brightness in every 10,000 cubic parsecs (equivalent to a cube just a bit larger than 20 parsecs along each edge). The brightest white dwarfs (small M_{bol}) are rare, less than one in every 100,000 cubic parsecs (a cube with edges of about 50 parsecs in length). Up to a limit ($M_{\text{bol}} = 15.5$), the number of white dwarfs per unit volume of the galaxy increases as the white dwarfs get fainter. The observations, however, show the dearth of very faint white dwarfs: only four white dwarfs are known with bolometric magnitudes larger than 15.5, and the number of such white dwarfs per unit volume of the galaxy drops precipitously. From Harris et al., *The Astrophysical Journal* (2006): 131, 571.

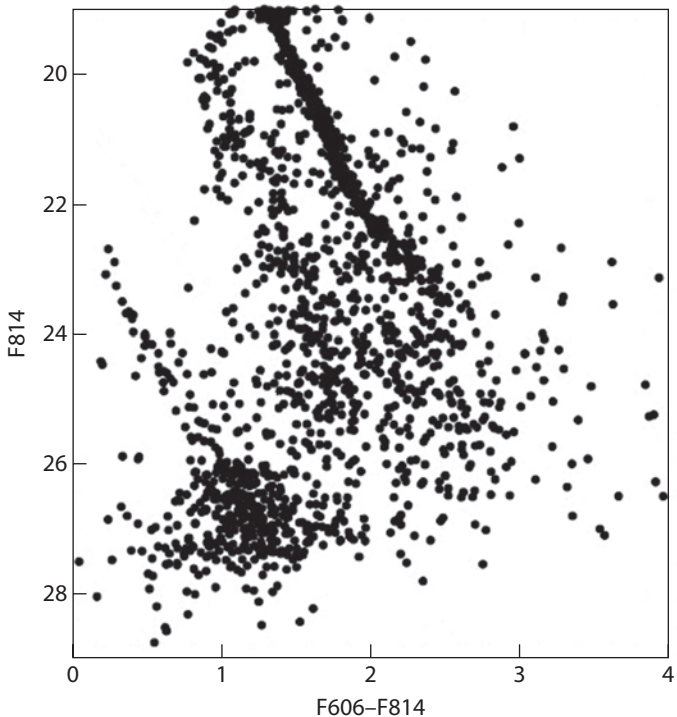


Figure 13.11. A plot of the colors of stars (x-axis) vs. the brightness of stars (y-axis) in the globular cluster M4, in data obtained from the Hubble Space Telescope. This plot is a color-magnitude diagram. The upper dark line, extending from the top-middle of the graph downwards and to the right, is the main sequence; the lower dark line, extending downwards from almost the left edge and at $F814 = 23.5$, is the white-dwarf cooling curve. In between, most of the scattered points mark out a main sequence of background stars unrelated to M4. The lower (faintest) limit to the white dwarfs seen at about magnitude 27.5 indicates the location on the plot of the coolest and oldest white dwarfs in this cluster. Their ages are calculated to be between 10 and 12 billion years. The x-axis is plotted in units labeled “F606–F814.” These are color filters used in Hubble Space Telescope observations that correspond, approximately, to green (F606) and red (F814). From Hansen et al., *The Astrophysical Journal Supplement* (2004): 155, 551.

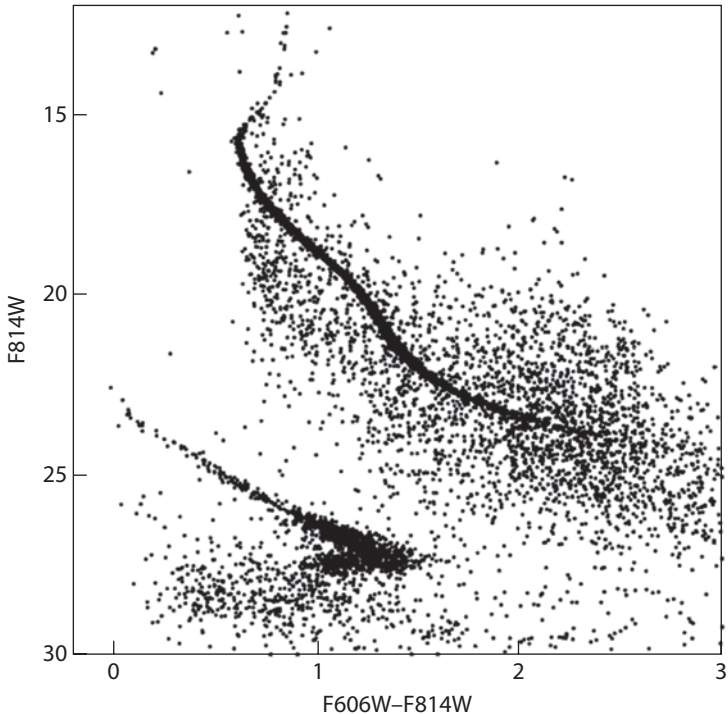


Figure 13.12. A plot of the colors of stars (x-axis) vs. the brightness of stars (y-axis) in data obtained from the Hubble Space Telescope for the globular cluster NGC 6397. The ages of the oldest, faintest white dwarfs in NGC 6397 are calculated to be about 11.5 billion years. From Hansen et al., *The Astrophysical Journal* (2007): 671, 380.

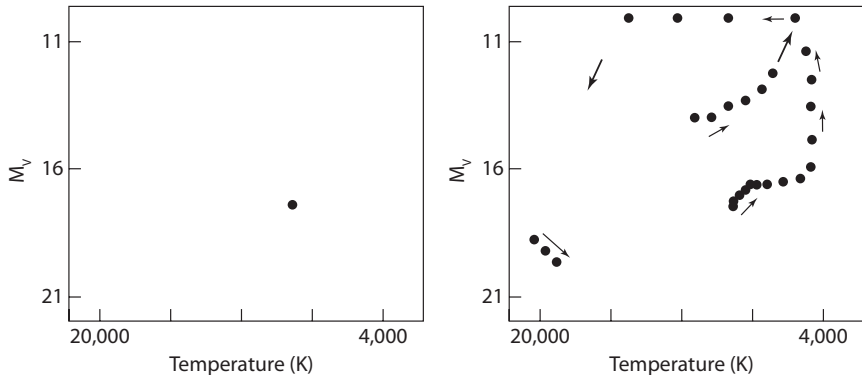


Figure 14.1. Left, a single point marks the temperature and absolute magnitude for a newborn star. Right, the progression of points reveals the changing surface temperature and absolute luminosity of this star as it ages. First it leaves the main sequence and climbs up the H-R diagram as a subgiant and then a red giant; then it drops down onto the horizontal branch and climbs back up to become a giant again; finally it puffs off its envelope as a planetary nebula and leaves behind a bare white dwarf that cools off and fades away.

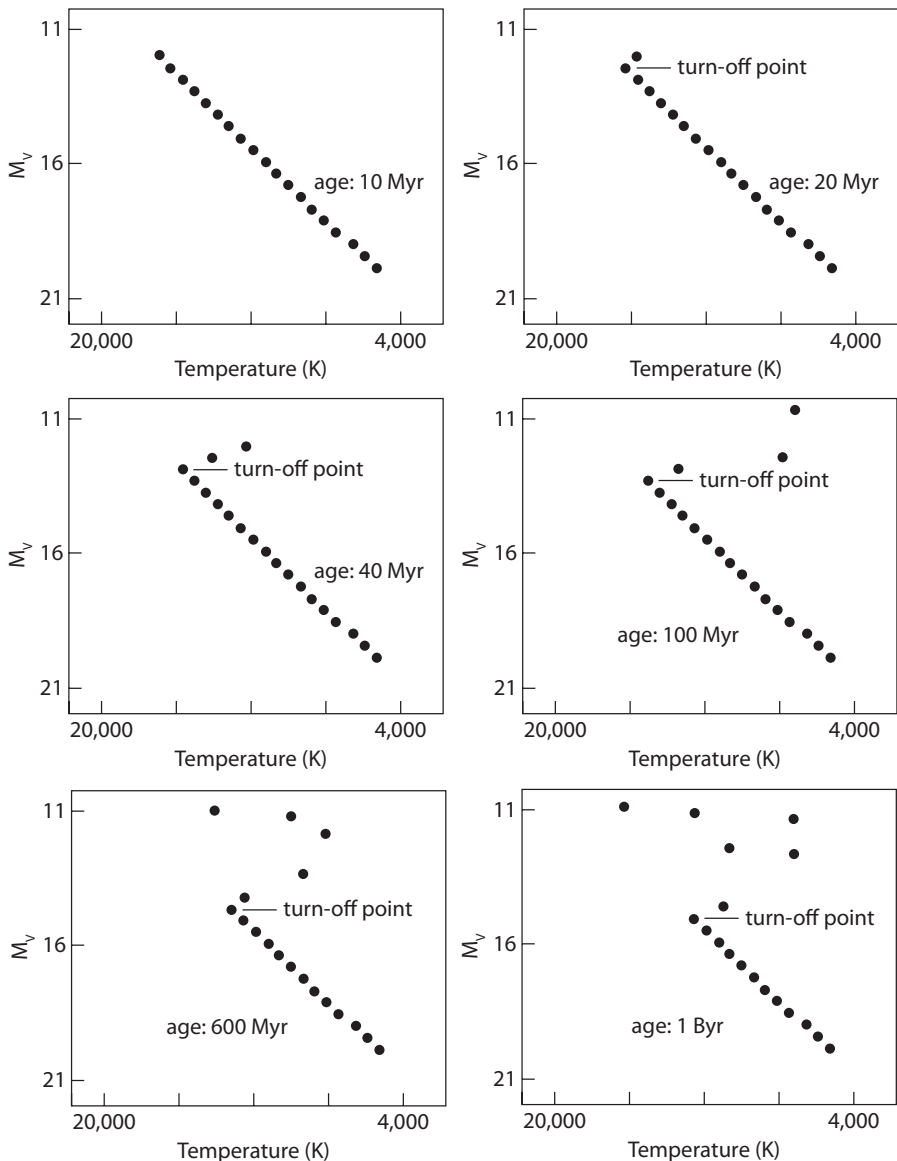


Figure 14.2. Sequence of cartoon snapshots of a star cluster at different ages. Initially (top left), stars of all masses are on the main sequence. After 20 million years (top right), the most massive star has exhausted the hydrogen in its core and has become a subgiant. The most luminous, most massive star still on the main sequence marks the turn-off point and age-dates the star cluster. In the lower panels, less massive stars begin to die and leave the main sequence, while the more massive stars progress to become red giants, planetary nebulae, and, finally, white dwarfs. In any single panel, a line connecting all the dots is called an *isochrone*.

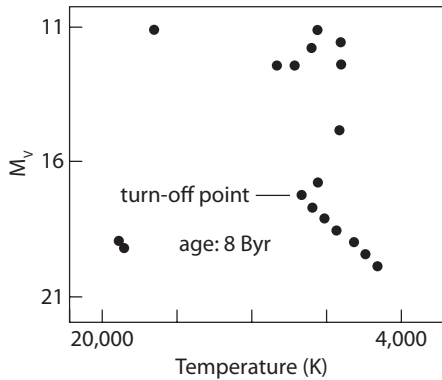
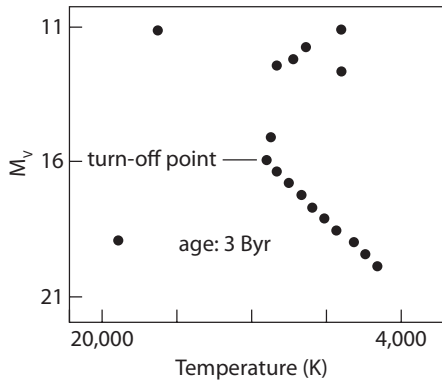


Figure 14.2. (Continued)

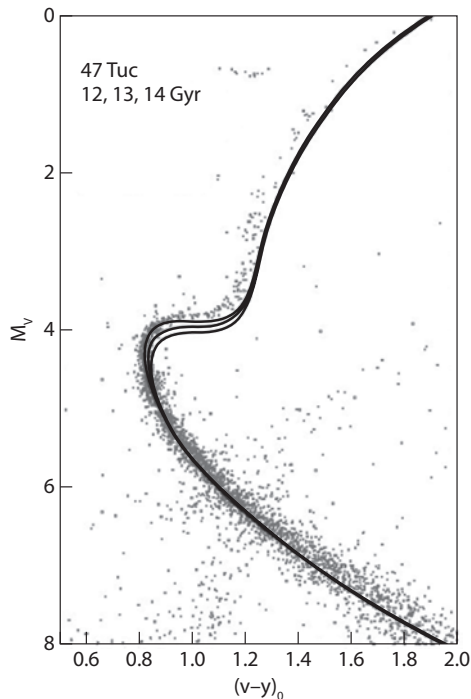
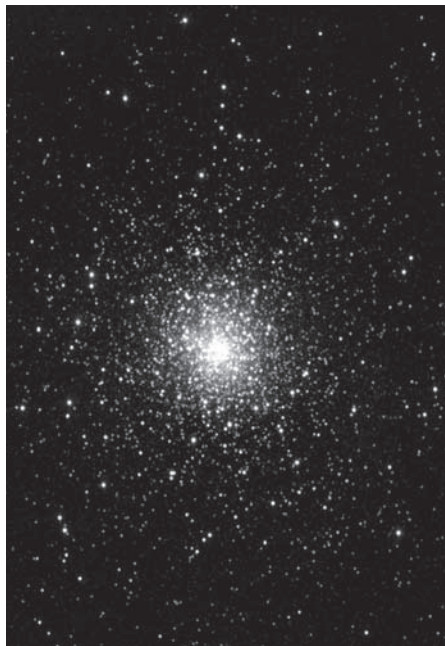


Figure 14.3. Left, image of globular cluster 47 Tuc. Right, H-R diagram (actually a color-magnitude diagram, where color is a proxy for temperature) of the stars in 47 Tuc, showing the main sequence, the turn-off point, the red giant branch, and the horizontal branch. The three isochrones delineate ages of 12 billion years (highest line, near $M_v = 4$), 13 billion years (middle line), and 14 billion years (lowest line). An age of about 12 billion years is the best fit. Atlas Image courtesy of 2MASS/UMass/IPAC-Caltech/NASA/NSF (left). From Grundahl et al., *Astronomy & Astrophysics* (2002): 395, 481 (right), reproduced with permission © ESO.

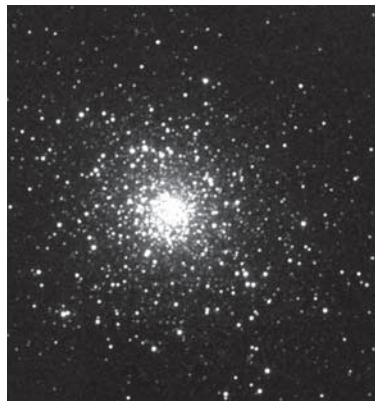
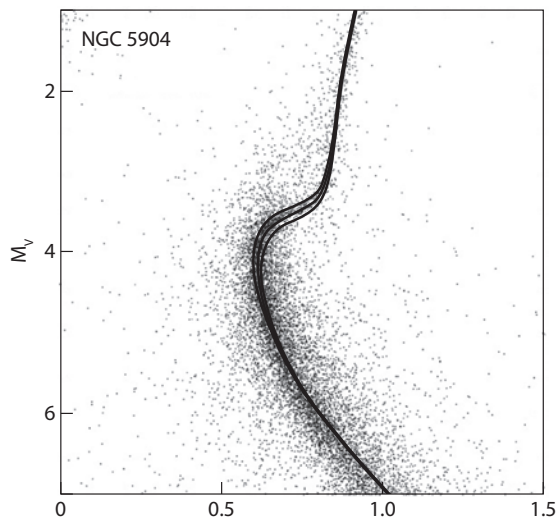
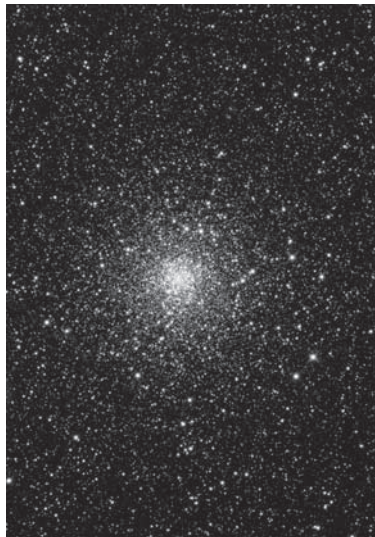
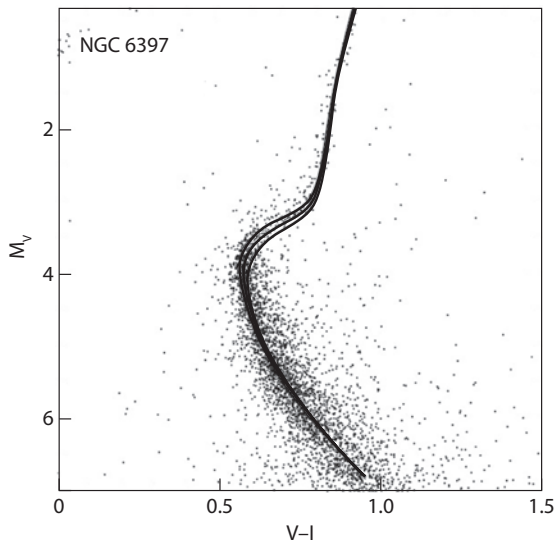


Figure 14.4. Top left, color-magnitude diagram for NGC 6397, with isochrones of 13 (topmost), 14 (middle), and 15 (bottom) billion years overlaid. Top right, Globular Cluster NGC 6397. Bottom left, color-magnitude diagram for NGC 5904, with isochrones of 13 (topmost), 14 (middle), and 15 (bottom) billion years overlaid. Bottom right, Globular Cluster NGC 6904. From Imbriani et al. *Astronomy & Astrophysics* (2004): 420, 625 (top left), reproduced with permission © ESO. Image courtesy of D. Verschate (Antilhue Observatory, Chile) and ESA/Hubble (top right). From Imbriani et al., *Astronomy & Astrophysics*, (2004): 420, 625 (bottom left), reproduced with permission © ESO. Atlas Image courtesy of 2MASS/UMass/IPAC-Caltech/ NASA/NSF (bottom right).

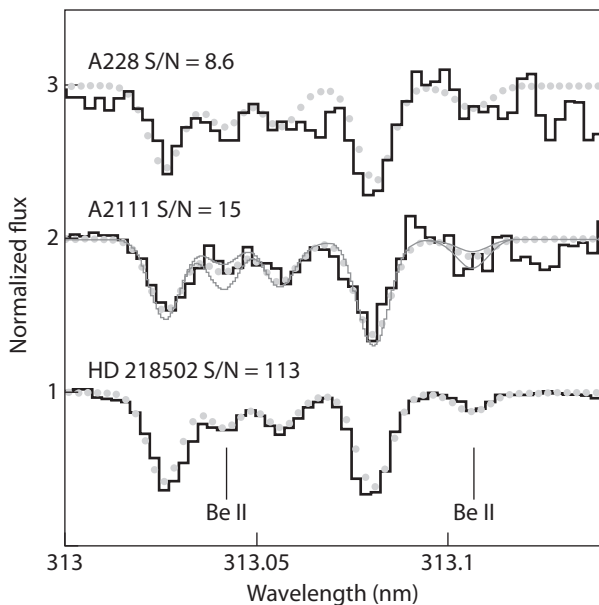
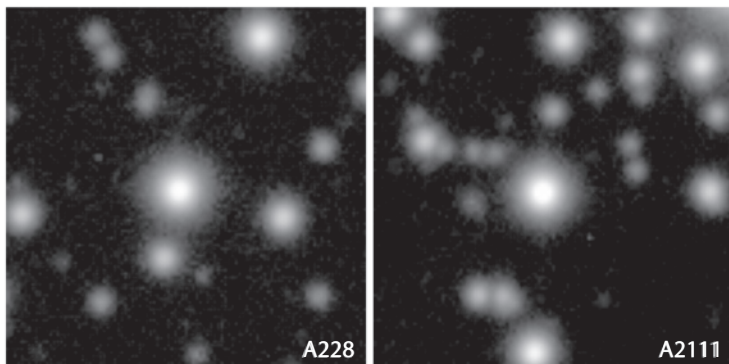


Figure 14.5. Top, two stars in the globular cluster NGC 6397 that are about to age off the main sequence. Bottom, three stars in NGC 6397 showing evidence of the presence of the element beryllium. Image courtesy of ESO (top). From Pasquini et al., *Astronomy & Astrophysics* (2004): 426, 651 (bottom), reproduced with permission © ESO.



Figure 15.1. Henrietta Swan Leavitt. Image courtesy of AIP Emilio Segre Visual Archives.

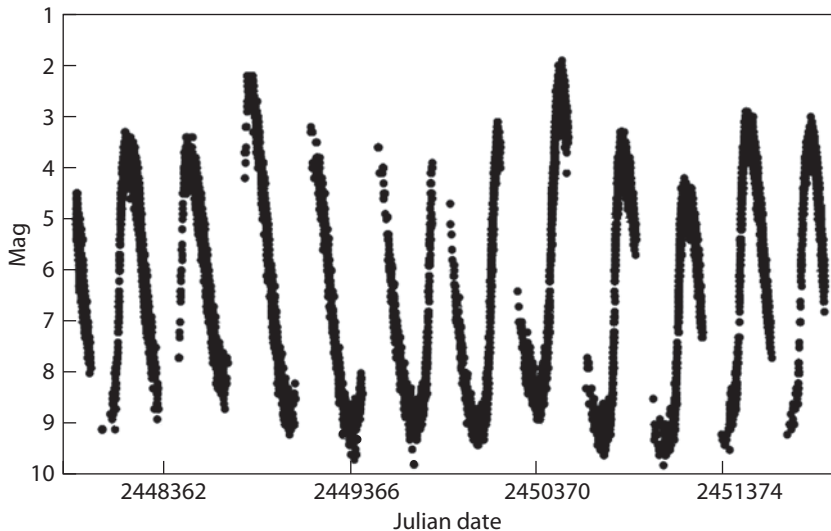


Figure 15.2. A light curve for the variable star Mira, with data from January 1, 1990 through December 31, 2000. The vertical axis numbers measure magnitudes, from one (brightest) to ten (faintest). Mira is known as a long-period variable star, because its light output increases from a minimum brightness of magnitude nine to ten to a maximum brightness of magnitude of two to three and then returns to magnitude nine to ten very regularly over a period of 332 days. Data courtesy of the AAVSO.

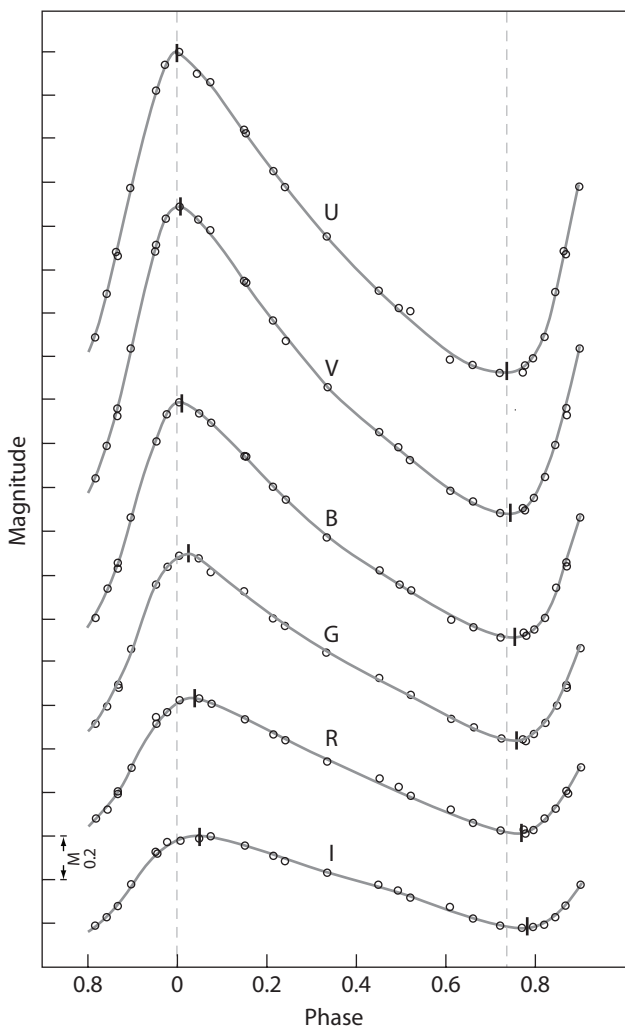


Figure 15.3. Light curve (time on the horizontal axis, difference in magnitude on the vertical axis) for Delta Cephei, as measured at six different colors, from the near ultraviolet (U) to the infrared (I). In visible light (V band), Delta Cephei changes by about 0.9 magnitudes from minimum to maximum (a factor of 2.3 in brightness) over a period of 5.366 days (1.0 units of Phase equals 5.366 days). Unlike the smooth pattern of stars like Mira, Cepheids have a very distinct pattern in their light curves that makes them easy to identify. Notice how Delta Cephei brightens from minimum (Phase = 0.8) to maximum (Phase 0.0) in just over one day but requires an additional four days to again fade to minimum brightness. From Stebbins, *The Astrophysical Journal*, (1945): 101, 47. Reproduced by permission of the AAS.

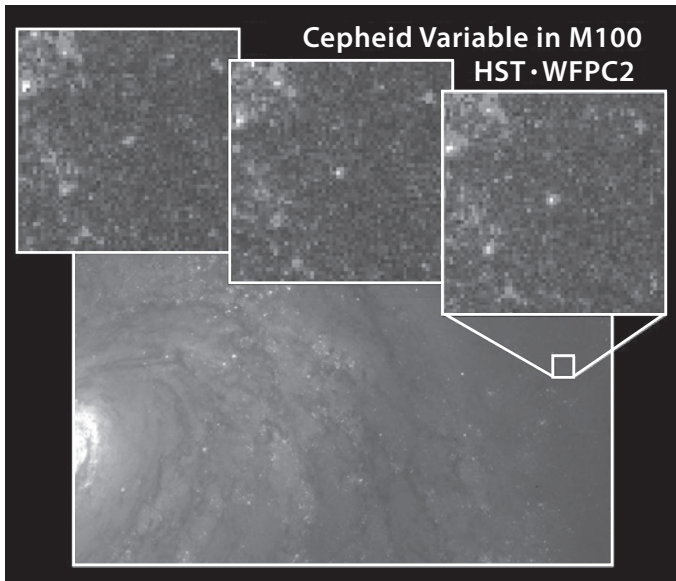


Figure 15.4. The three upper panels show Hubble Space Telescope close-ups of a region in the galaxy M100 in which a Cepheid variable star gets successively brighter (from left to right). Image courtesy of Dr. Wendy L. Freedman, Observatories of the Carnegie Institution of Washington, and NASA.

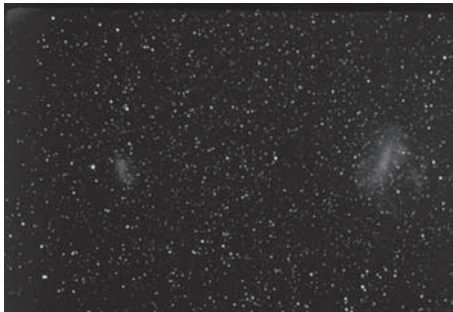


Figure 15.5. Photograph of the Large (left) and Small (right) Magellanic Clouds. Image courtesy of William Keel, University of Alabama at Tuscaloosa.

1777 VARIABLES IN THE MAGELLANIC CLOUDS.

BY HENRIETTA S. LEAVITT.

Figure 15.6. Henrietta Leavitt was able to publish her 1908 paper in the *Annals of Harvard College Observatory* under her own name. Her follow-up paper would be published in 1912 under the sole authorship of Edward Pickering. From Leavitt, *Annals of Harvard College Observatory* (1908): 60, 87.

TABLE VI.

PERIODS OF VARIABLES IN THE SMALL MAGELLANIC CLOUD.

Harvard No.	Max.	Min.	Range.	Epoch.	Period.	Min. to Max.	Average Dev.	Earliest Observation.	No. Periods.	No. Plates.
					<i>d.</i>	<i>d.</i>				
818	13.6	14.7	1.1	4.0	10.336	1.7	.12	1890	566	44
821	11.2	12.1	0.9	97.	127.	49.	.06	1890	45	89
823	12.2	14.1	1.9	2.9	31.94	3.	.13	1890	184	56
824	11.4	12.8	1.4	4.	65.8	7.	.12	1889	94	83
827	13.4	14.3	0.9	11.6	13.47	6.	.11	1890	448	60
842	14.6	16.1	1.5	2.61	4.2897	0.6	.06	1896	843	26
1374	13.9	15.2	1.3	6.0	8.397	2.	.10	1893	574	42
1400	14.1	14.8	0.7	4.0	6.650	1.	.11	1893	724	42
1425	14.3	15.3	1.0	2.8	4.547	0.8	.09	1893	1042	33
1436	14.8	16.4	1.6	0.02	1.6637	0.3	.10	1893	2859	22
1446	14.8	16.4	1.6	1.38	1.7620	0.3	.09	1896	2052	21
1505	14.8	16.1	1.3	0.02	1.25336	0.2	.10	1896	2335	25
1506	15.1	16.3	1.2	1.08	1.87502	0.3	.09	1896	1560	23
1646	14.4	15.4	1.0	4.30	5.311	0.7	.06	1896	681	24
1649	14.3	15.2	0.9	5.05	5.323	0.7	.10	1893	894	32
1742	14.3	15.5	1.2	0.95	4.9866	0.7	.07	1893	954	28

Figure 15.7. Table VI from Leavitt's 1908 paper, which shows the first evidence for the period-luminosity relationship, contains the key information that enabled astronomers to discover the nature of the spiral nebulae and then to step out into the distant universe and, ultimately, to discover the expanding universe and calculate its age. Of the sixteen stars listed according to their Harvard number (column 1), those with the shortest periods (column 6) are the faintest (the largest maximum and minimum magnitudes; columns 2 and 3), while those with the longest periods are brightest (the smallest maximum and minimum magnitudes). Star 821, for example, has a very long period (127 days) and is very bright (maximum brightness of magnitude 11.2), while star 1505 has a very short period (1.25336 days) and is much fainter (maximum brightness of magnitude 14.8). From Leavitt, *Annals of Harvard College Observatory* (1908): 60, 87.

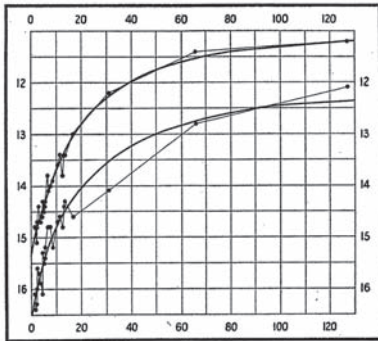


FIG. 1.

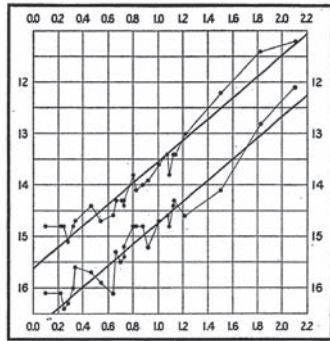


FIG. 2.

Figure 15.8. Henrietta Leavitt's plots of the periods of "cluster variables" in the Small Magellanic Cloud (x-axis) versus the brightnesses of those stars (y-axis). Each plot shows two lines, the top line indicating the maximum brightness (minimum apparent magnitude) of the stars and the bottom line the minimum brightness (largest apparent magnitude) of the stars. The left plot marks the period of variability for these stars in days, from 0 to 140 days (x-axis); the right plot marks the period using the logarithm of the number of days (x-axis). These plots reveal the simple relationship between the magnitude and period of Cepheid variable stars that has become known as the *period-luminosity relationship*. From Pickering, *Harvard College Circular* (1912): 173.

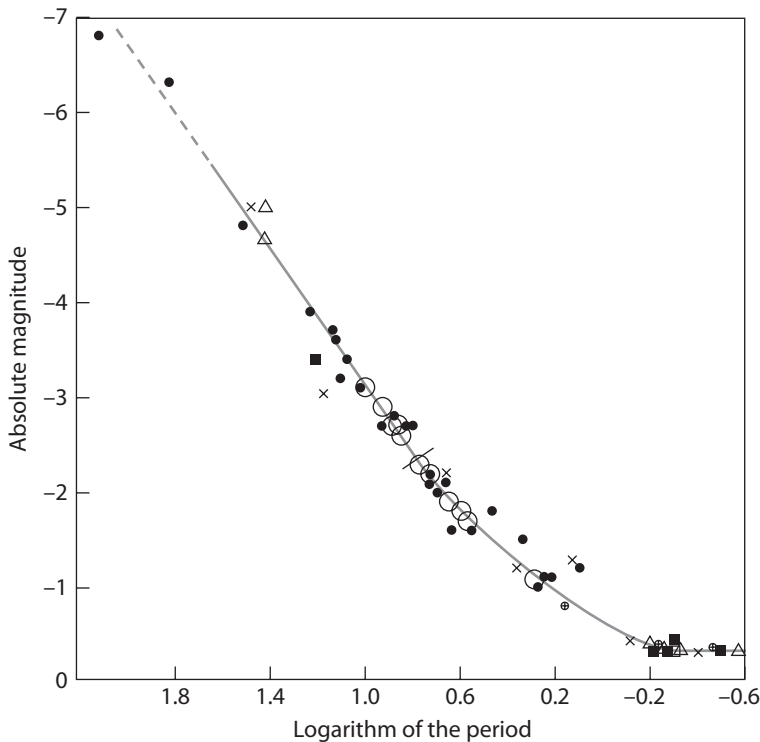


Figure 15.9. Harlow Shapley's 1918 "luminosity-period curve of Cepheid variation." This plot shows the logarithm of the period (negative numbers are periods less than one day; 0.0 is a period of 1 day; +1.0 is a period of 10 days; +2.0 would be a period of 100 days) along the x-axis and the (median) absolute magnitude for each star on the y-axis (0 is faintest; -7 is brightest). The Cepheids with the longest periods are brightest, those with the shortest periods are faintest. From Shapley, *The Astrophysical Journal* (1918): 48, 89.

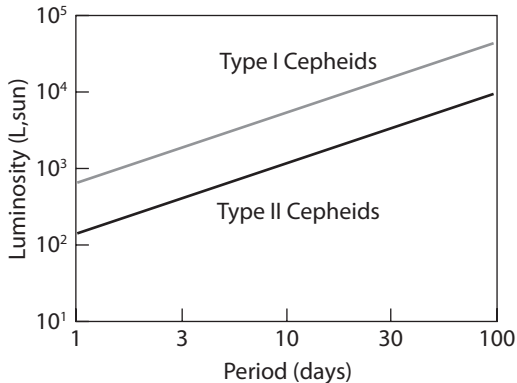


Figure 15.10. A modern period-luminosity diagram showing the two types of Cepheids. Type I Cepheids are about four times brighter than Type II Cepheids having the same period.

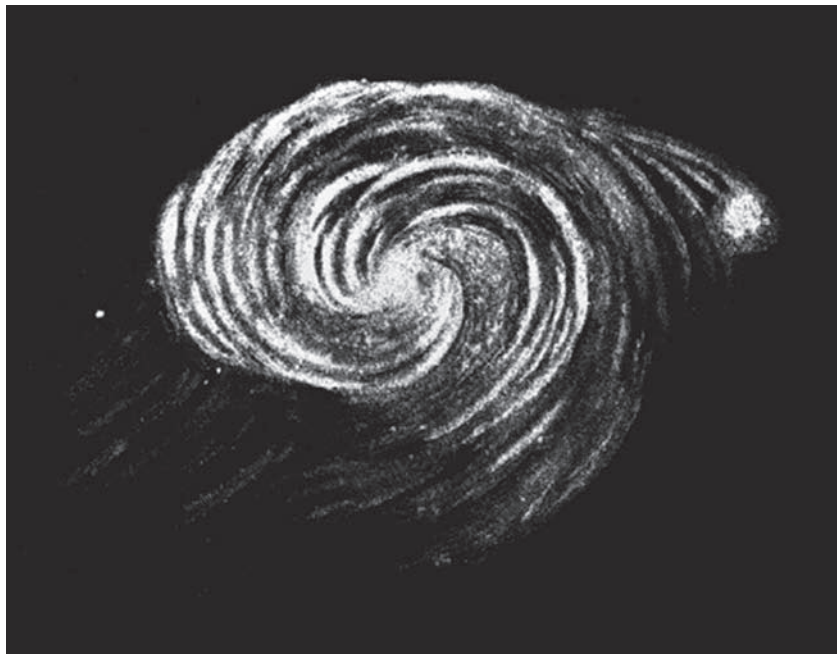


Figure 16.1. Top, sketch of the Whirlpool Galaxy (M51) made by Lord Rosse in 1845. Bottom, Hubble Space Telescope image of M51. Image courtesy of NASA, ESA, S. Beckwith (STScI), and the Hubble Heritage team (STScI/AURA).

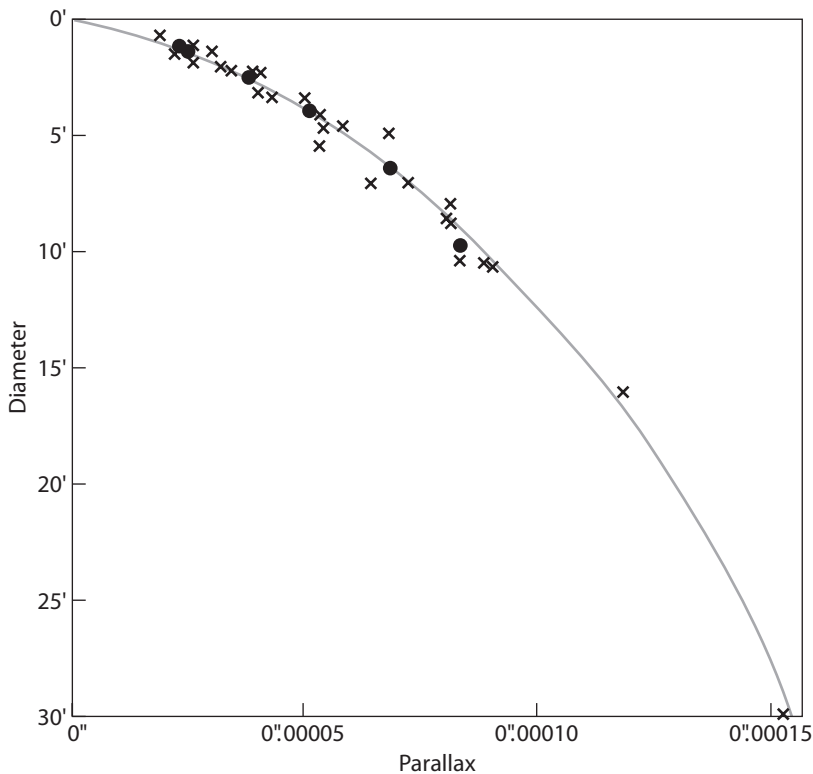


Figure 16.2. Shapley's parallax-diameter correlation for globular clusters. Globular clusters that subtend smaller angular sizes in the sky (higher on graph) have smaller parallaxes (left on graph) and therefore lie at greater distances than the globular clusters with larger angular sizes. From Shapley, *The Astrophysical Journal* (1918): 48, 154.

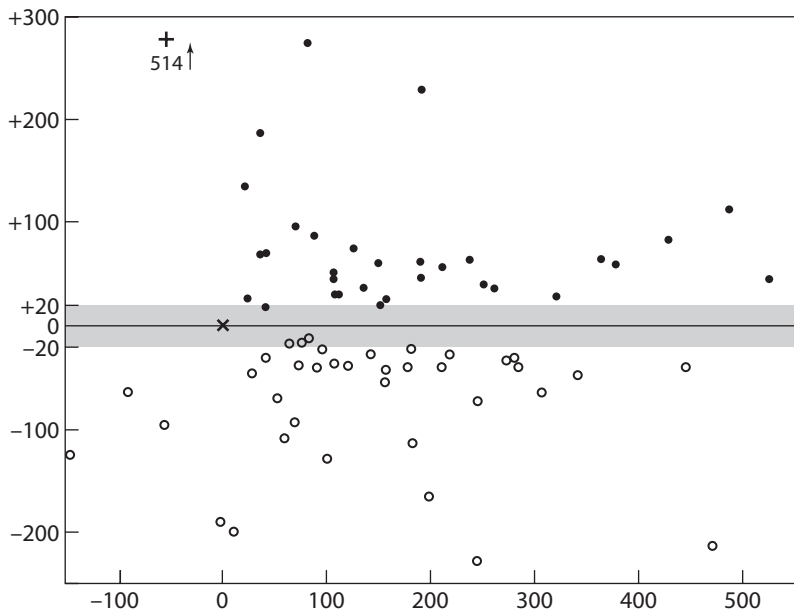


Figure 16.3. Shapley's map of the positions of the known globular clusters. The vertical axis marks distance above the midplane of the Milky Way, while the horizontal axis marks the distance from the Sun. All units are in increments of 100 parsecs, so that one square (100 units) equals a distance of 10,000 parsecs. The Sun is at the position $x = 0$ and $y = 0$. Shapley's map shows that all but five of the globular clusters are on one side of the sky, placing the Sun near the edge of this distribution. The clusters are also distributed equally above and below the galactic midplane. From Shapley, *The Astrophysical Journal* (1918): 48, 154.

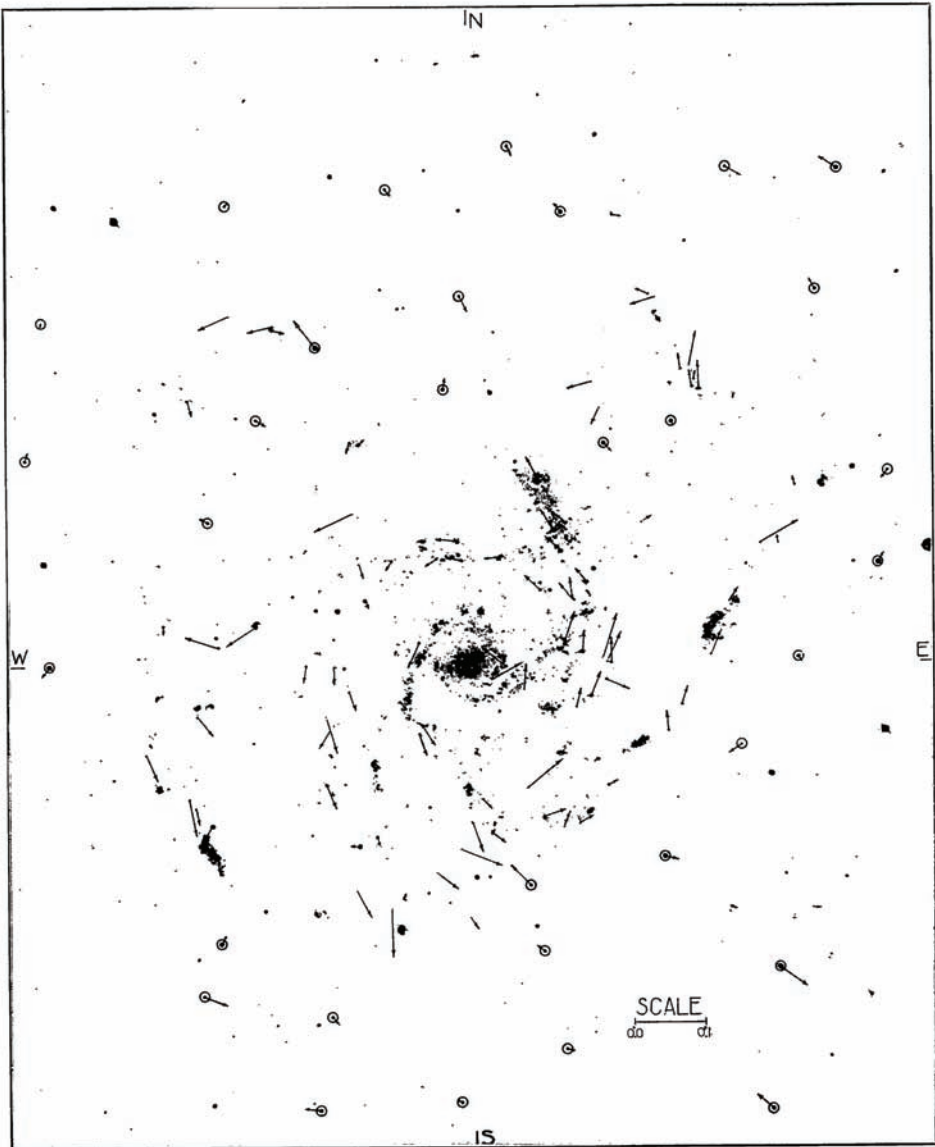


Figure 16.4. Van Maanen's measurements showing the apparent rotation of stars in M101. The arrows indicate the direction and magnitude of the (incorrectly) measured annual motions. From van Maanen, *The Astrophysical Journal* (1916): 44, 210.

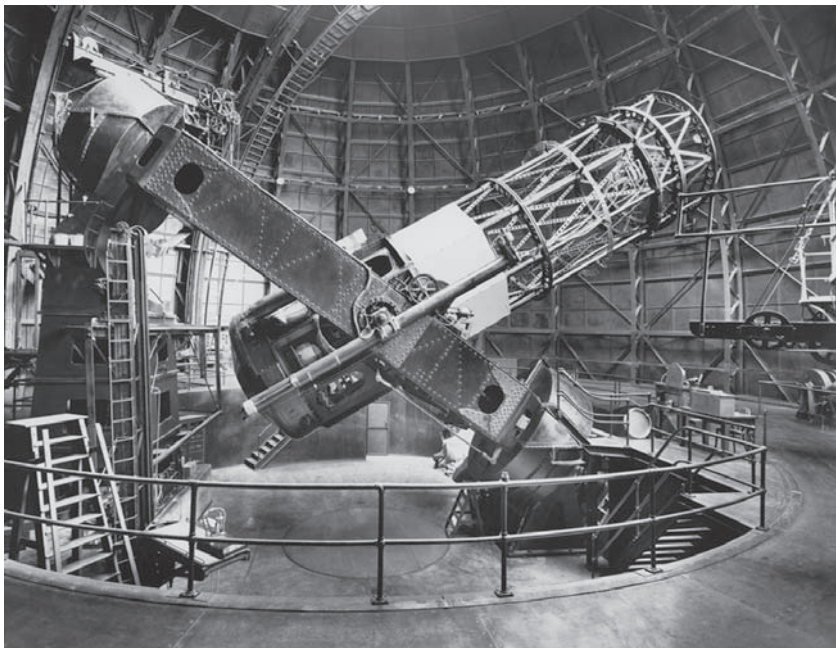


Figure 17.1. The Mount Wilson Observatory's 100-inch telescope, c. 1940. Hubble's chair is visible to the left. Image courtesy of the Huntington Library, San Marino, California.



Figure 17.2. Infrared image of NGC 6822. NGC 6822 is the first galaxy identified by Edwin Hubble as an object clearly outside of the Milky Way. Image courtesy of 2MASS/UMass/IPAC-Caltech/NASA/NSF.

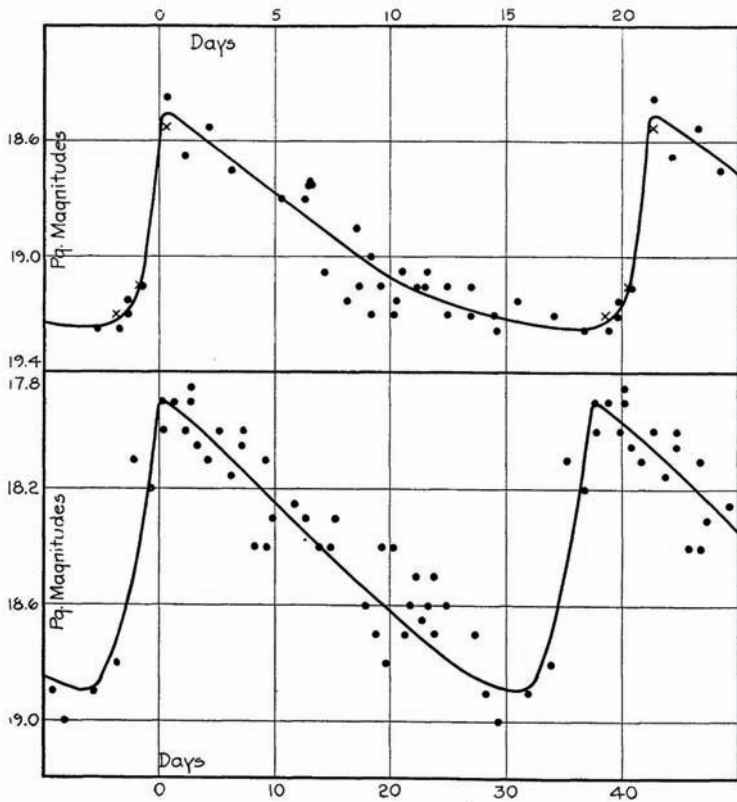


Figure 17.3. Light curves for two Cepheids in NGC 6822, presented by Hubble in his groundbreaking 1925 paper. From Hubble, *The Astrophysical Journal* (1925) 62, 409. Reproduced by permission of the AAS.

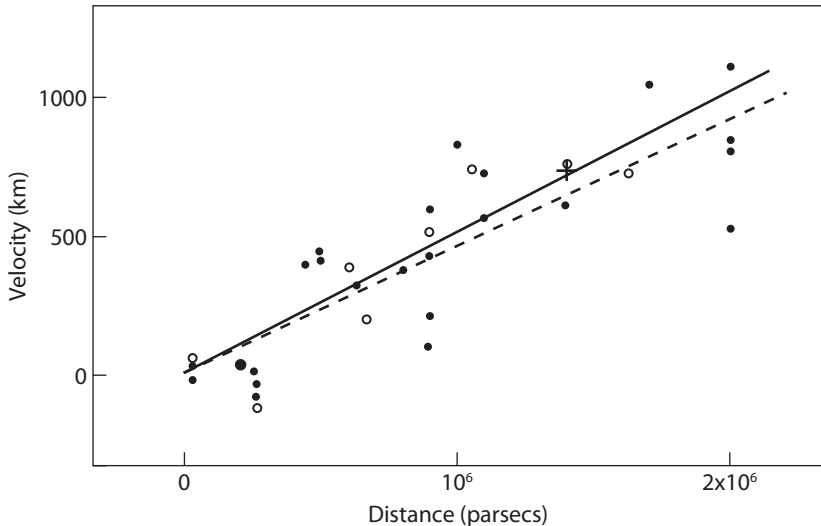


Figure 19.1. Hubble's 1929 plot showing that the distance to a galaxy is directly proportional to the redshifted velocity of that galaxy. Distance is measured along the x-axis, with each box representing one million parsecs. Velocity is measured along the y-axis (each box representing a speed of 500 km per second. Note that the original labels on the y-axis have incorrect units and, as we will see in Chapter Twenty, the x-axis has the wrong values). From Hubble, *Proceedings of the National Academy of Science* (1929): 15, 169.

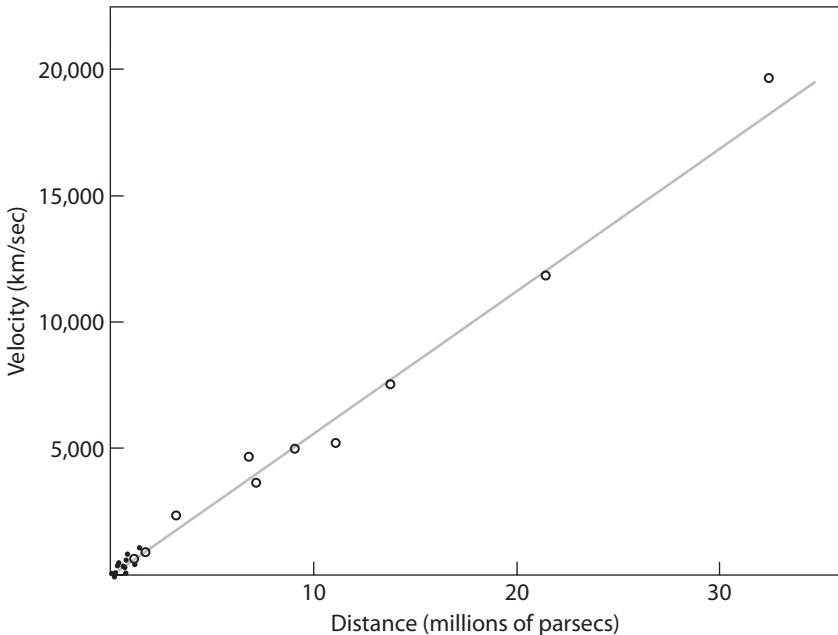


Figure 19.2 Hubble's velocity-distance relationship in 1931. Note that the 1929 measurements extended out to a distance of only two million parsecs, i.e., the leftmost fifth of the leftmost and lowest box. Each open circle represents the mean value for a cluster of galaxies. From Hubble and Humason, *The Astrophysical Journal*, (1931): 74, 43.

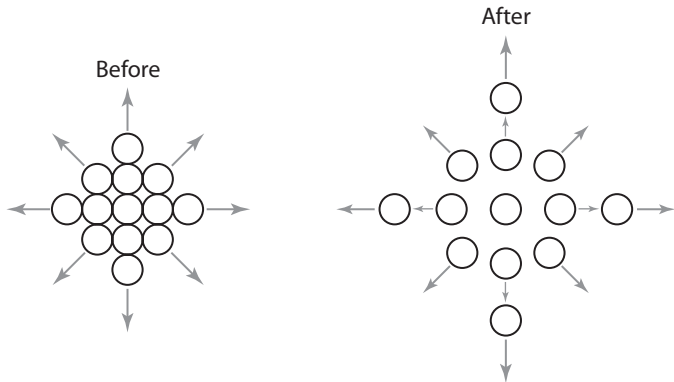


Figure 19.3. Illustration of exploding bomb fragments. Left, all fragments begin at (or near) the center. Right, after the explosion, the fastest moving fragments have moved the greatest distance from the center, while the objects at the center are not moving at all.

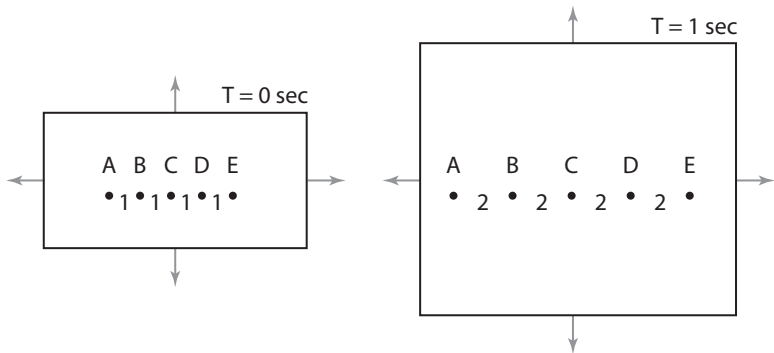


Figure 19.4. Illustration of Hubble's law. Left, at time 0 seconds, we have a piece of paper with five dots (labeled A, B, C, D, and E). Each dot is separated from the next closest dot by one unit of distance (e.g., one meter). Right, one second later, our piece of paper has been stretched in all directions so that it has doubled in size. The distance from A to B has doubled from one to two meters. The distance from A to E has doubled from four to eight meters. An observer at dot A would discover that dot B is moving away from dot A at a speed of one meter per second, while dot E is moving away at a speed of four meters per second. An observer at any position would find that the other dots are moving away from that position with speeds that are directly proportional to their distances from that position.



Figure 20.1. Walter Baade. Image courtesy of the Huntington Library, San Marino, California.

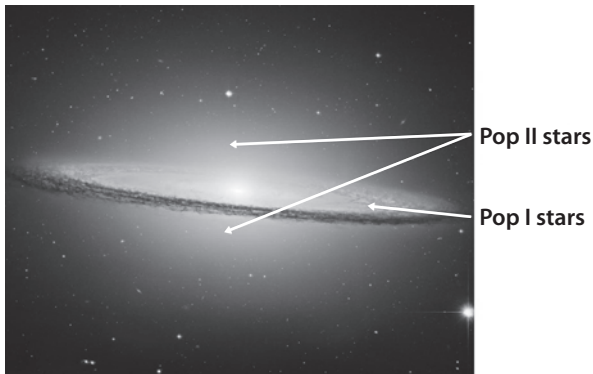


Figure 20.2. The Sombrero Galaxy (M104). Walter Baade discovered that spiral galaxies have two distinct populations of stars: Pop I stars are in the galactic disk and include many young blue stars, while Pop II stars are exclusively old red stars in the galactic halo. Image courtesy of NASA and the Hubble Heritage team (STScI/AURA).

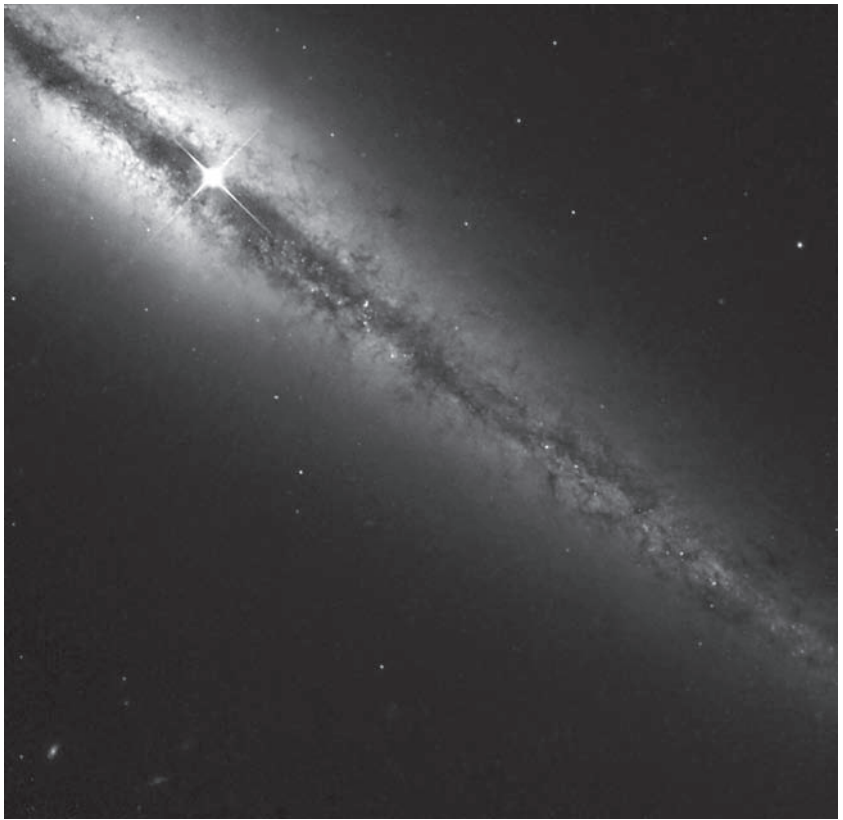


Figure 20.3. Edge-on spiral galaxy NGC 4013. In 1930, Robert Trumpler proved that interstellar dust exists and both dims and reddens starlight from distant objects. The dark lanes in spiral galaxies are due to the presence of enormous amounts of dust between the stars. Image courtesy of NASA and the Hubble Heritage team (STScI/AURA).

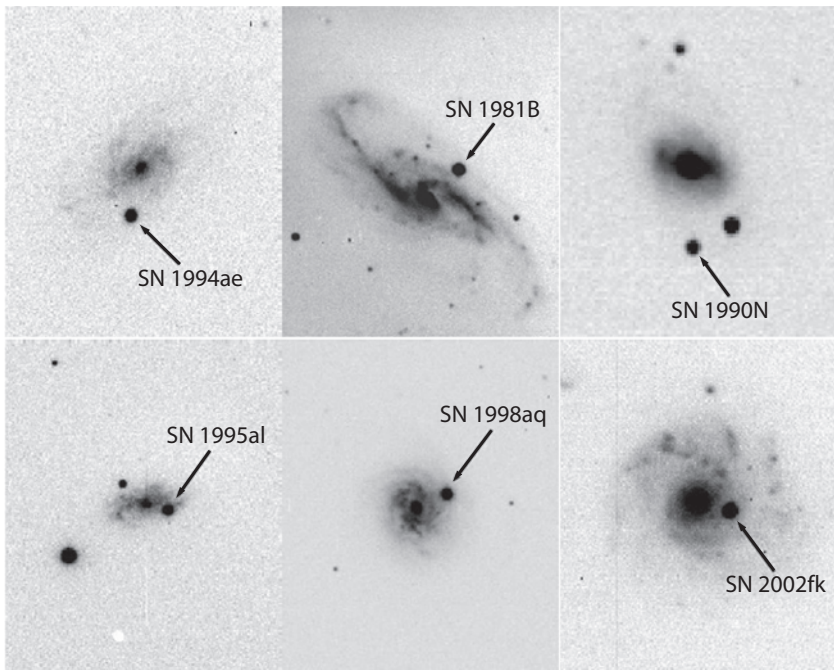


Figure 21.1. Optical images of six supernovae near their peak brightnesses. In each of these images, the supernova is seen when its brightness is comparable to that of its host galaxy. From Riess et al., *The Astrophysical Journal* (2009): 699, 539.

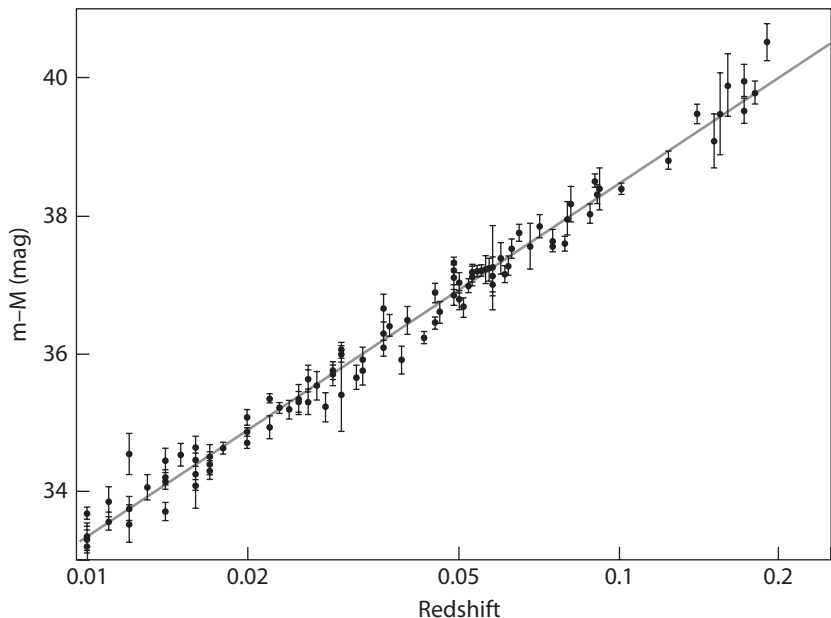


Figure 21.2. Observations of supernovae at relatively low redshift (low z), plotted with redshift versus distance. (The difference between the apparent and absolute magnitudes, plotted on the y-axis, can be thought of as a proxy for distance.) The straight line through all the data points indicates that the inverse square law for light applies for objects out to redshifts of $z = 0.2$, and therefore that the expansion rate of the universe is very constant over the time period measured by these observations. From Perlmutter and Schmidt, “Supernovae and Gamma-Ray Bursters,” in *Lecture Notes in Physics*, K. Weiler, ed. (2003): 598, 195. Reproduced by permission of Springer Publishing.

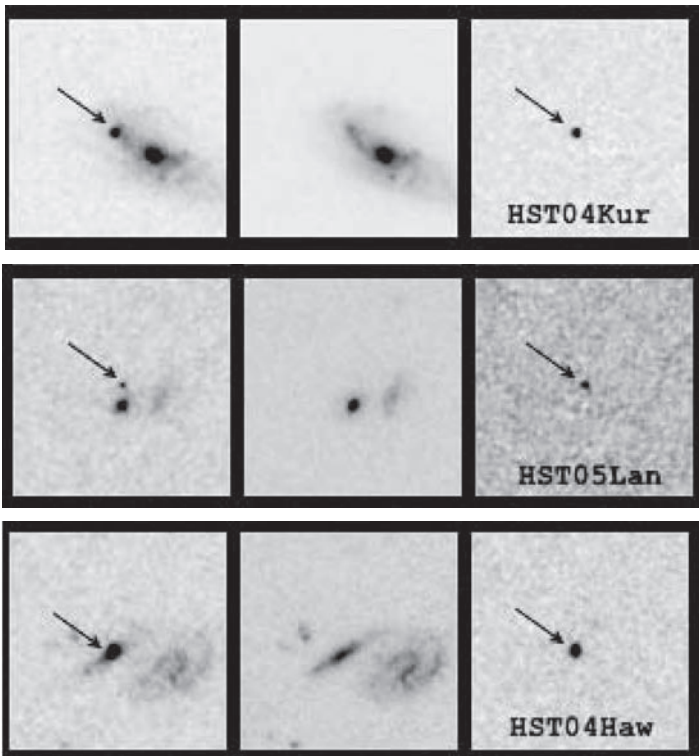


Figure 21.3. Discovery images of supernovae in the galaxies HST04Kur, HST05Lan, and HST04Haw. The left panels show images after the supernovae exploded, the center panels images taken before the supernovae exploded, and the right panels the differences between these pairs of images (each “before” image is subtracted from its partner “after” image). From Riess et al., *The Astrophysical Journal*, (2007): 659, 98, and the High- z team.

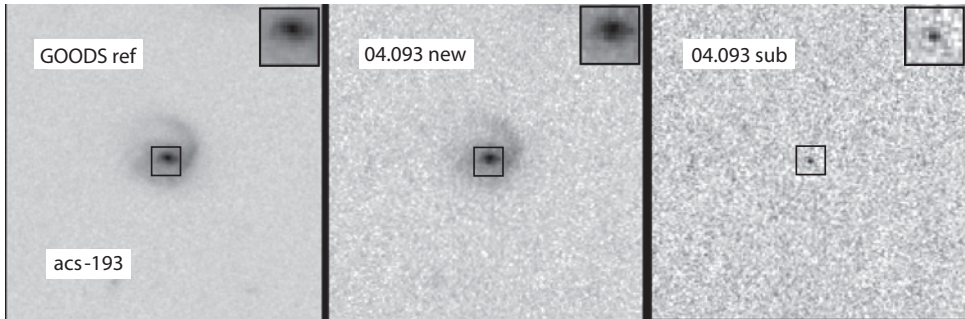


Figure 21.4. Discovery images of a supernova in the galaxy acs-193. The left panel shows an image of acs-193 taken before the supernova exploded, the center panel an image taken after the supernova exploded, and the right panel the difference between these two images (the “before” image subtracted from the “after” image). In this case, the supernova exploded very nearly at the center of the galaxy, making it very difficult to identify the presence of the supernova except in the third image. Images courtesy of Robert Knop.

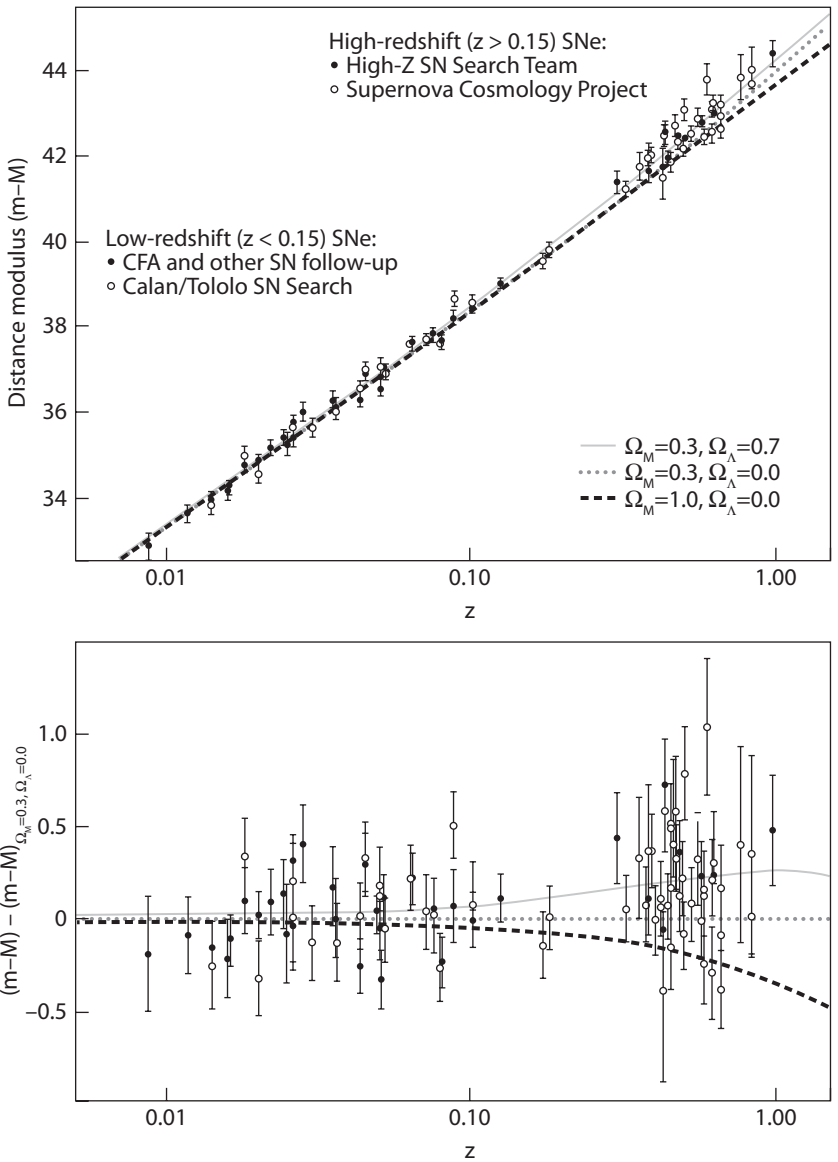


Figure 21.5. Observations of supernovae at high redshift (above $z = 0.15$). The data from the previous plot fits onto the left side of this plot. The thick dashed line marks where the supernovae were expected to be found on this plot: given Hubble's law for smaller redshifts, a given redshift predicts the distance of any supernova. Top panel,

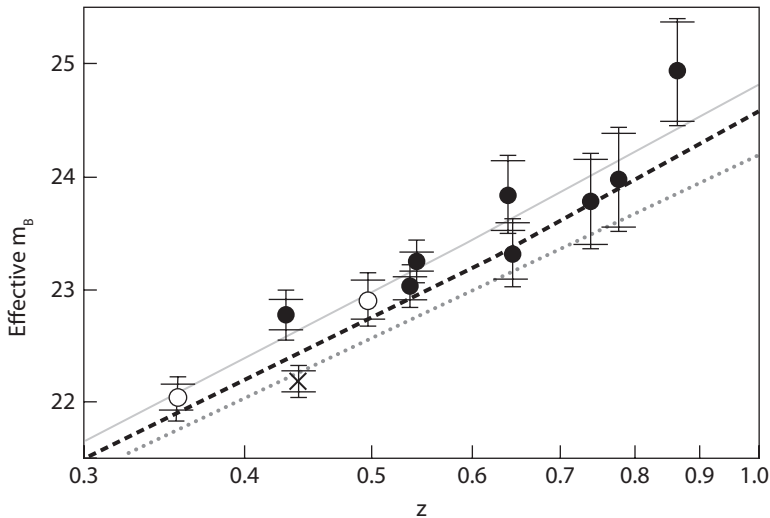


Figure 21.6. Brightness versus redshift plot for supernovae with redshifts from 0.3 to 0.9 discovered with the Hubble Space Telescope by the Supernova Cosmology Project team. The lower (dotted) line shows where the supernovae would be in a coasting universe. The solid (top) line is the best fit to these data. The actual supernovae measurements show that they are fainter (the effective apparent magnitude) than expected at every redshift. Image from Knop et al., *The Astrophysical Journal* (2003): 598, 102.

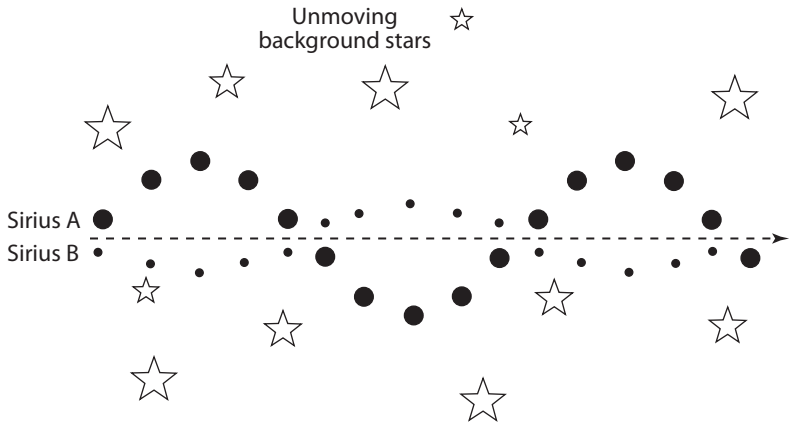


Figure 22.1. Illustration of the motion of a binary star system (here Sirius A and B) as they slalom past the fixed stars over a time period that spans many decades. For the first twenty years after the curved-path motion of Sirius A, with respect to the background stars, was first detected, even the most powerful telescopes were not strong enough to permit observers to detect the presence of Sirius B.



Figure 22.2. The Coma Cluster, a prototypical dense cluster of galaxies. This was the cluster studied by Fritz Zwicky in 1933. Image courtesy of the Sloan Digital Sky Survey Collaboration, www.sdss.org.

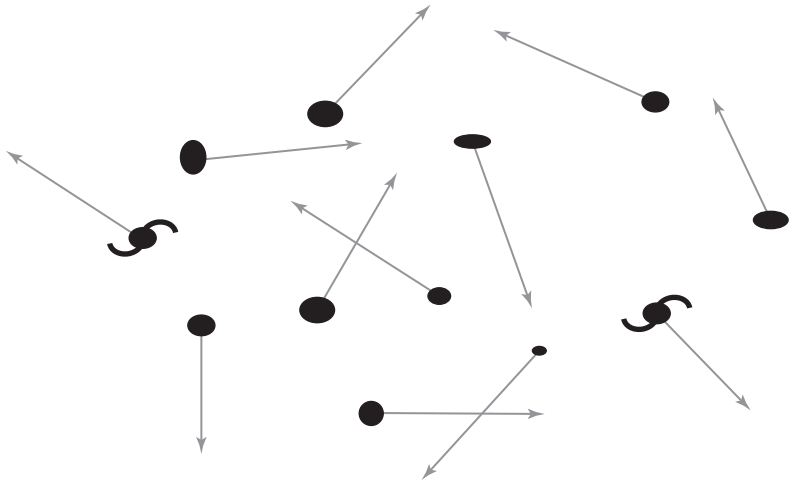


Figure 22.3. Illustration of the motions of galaxies in the Coma Cluster. Zwicky found that their velocities were so high that the galaxies should escape from the cluster.

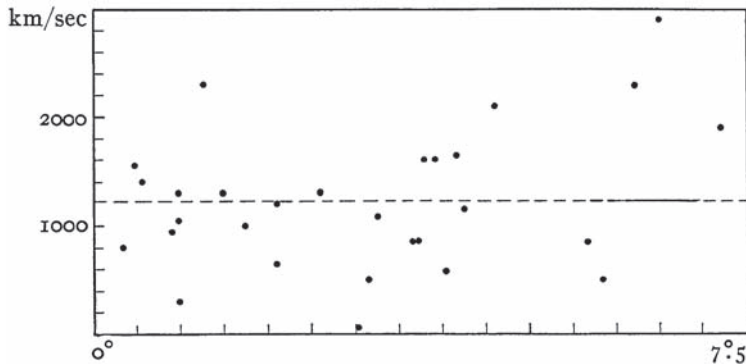


Figure 22.4. The distribution of velocities of thirty galaxies in the Virgo Cluster, as presented by Sinclair Smith in 1936. Some individual galaxies are moving as fast as 1,500 kilometers per second relative to the mean velocity (dashed line) of 1,225 kilometers per second. From Sinclair Smith, *The Astrophysical Journal* (1936): 83, 23. Reproduced by permission of the AAS.

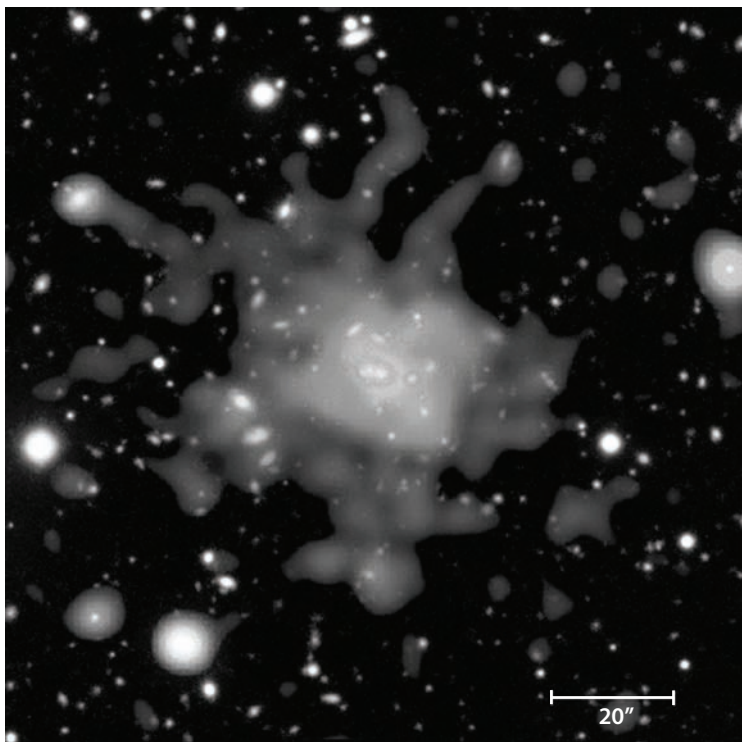


Figure 22.5. This Chandra telescope image of the galaxy cluster RDCS 1252.9-2927 shows the emission of X-rays from 70-million-degree-Celsius gas (seen as the gray and white fuzz and blobs). The X-ray image is superimposed on a visible-light image of the cluster (all of the small dots and smudges are the galaxies seen in visible light). X-ray data indicate that this cluster formed more than 8 billion years ago and has a mass at least 200 trillion times that of the Sun. X-ray image courtesy of NASA/CXC/ESO/P. Rosati et al. Optical image courtesy of: ESO/VLT/P.Rosati et al.

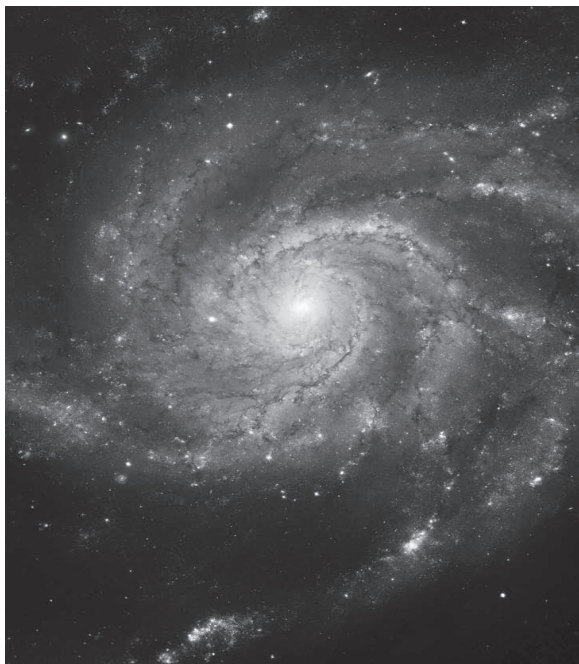
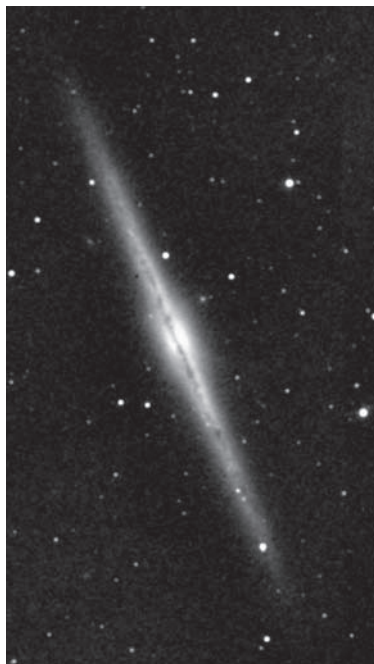


Figure 22.6. Two spiral galaxies. Left, NGC 891. This galaxy is viewed edge on. Right, M101, the Pinwheel galaxy. This image shows how a spiral galaxy looks when viewed from directly above its midplane. Images courtesy of NASA and 2MASS (left), European Space Agency & NASA (right).

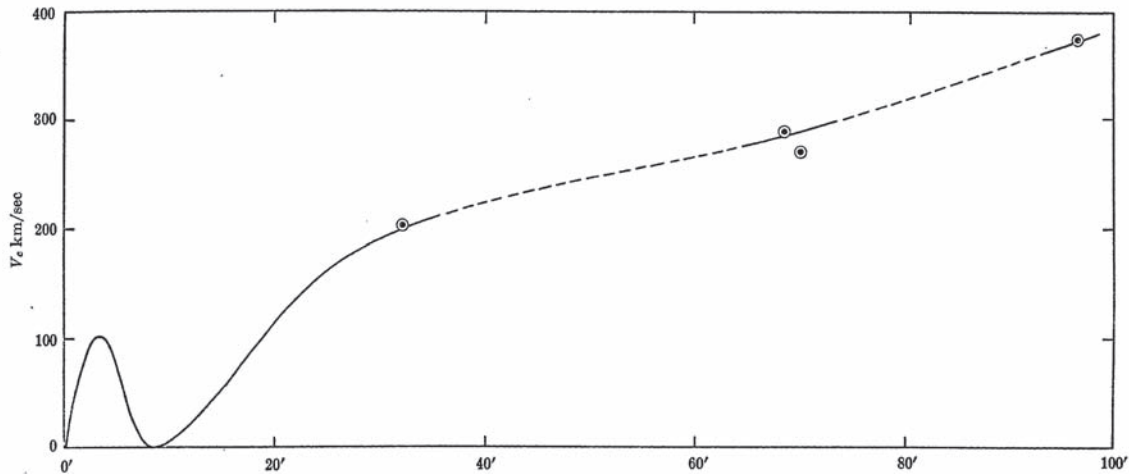


Figure 22.7. Horace Babcock's rotation curve for the Andromeda Galaxy. The vertical axis indicates the velocities of the observed stars, the horizontal axis the distance of those stars from the center of the galaxy (in minutes of arc). Within a few minutes of arc of the center, the orbital velocities increase rapidly with distance, indicating the presence of additional mass with increasing distance from the center. Then the orbital velocities decrease rapidly, indicating that no additional mass is being added to the total galaxy mass over this distance interval. From about 10' of arc (600 pc) out to 100' of arc (6,000 pc), the orbital velocities increase steadily, indicating that a great deal of unseen mass is spread through this part of the galaxy. From Horace Babcock, *Lick Observatory Bulletin* (1939): 498.

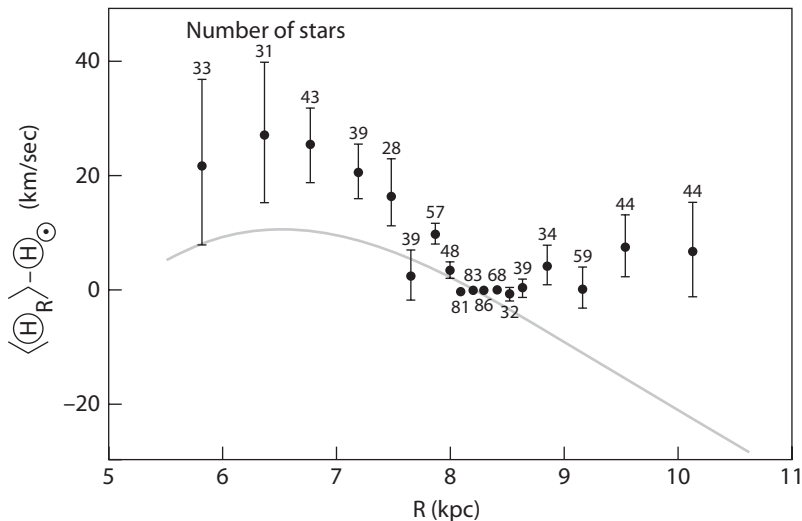


Figure 22.8. Vera Rubin's 1962 rotation curve for the Milky Way Galaxy. The vertical axis indicates the velocities of the stars in comparison to the velocity of the Sun, the horizontal axis the distance from the center of the galaxy (in kiloparsecs). Numbers along the top of the chart indicate the number of stars observed for each data point on the plot. The data show a flat rotation curve from 8 kpc outwards. The solid curve shows the rotation curve for the galaxy based on 1954 measurements of radio signals emitted by Milky Way hydrogen gas clouds within eight kpc of the center, which these data match reasonably well. 1956 models showing what the rotation curve was expected to look like at distances from the center greater than eight kpc clearly do not match these data. From Rubin et al., *The Astronomical Journal*, (1962): 67, 491.

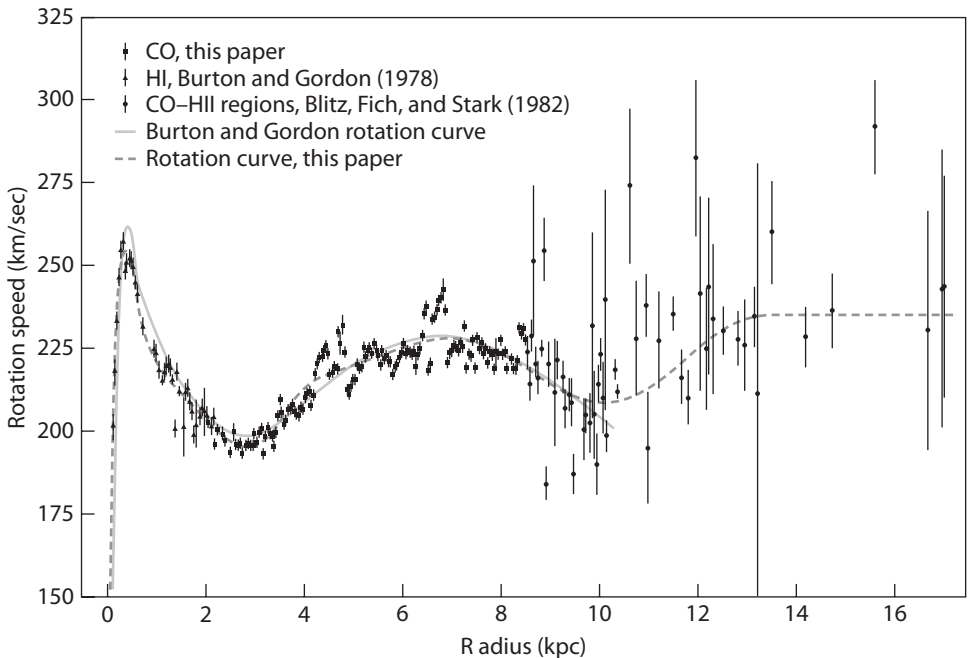


Figure 22.9. Dan Clemens' 1985 rotation curve for the Milky Way, with measurements extending nearly to the center of the galaxy and more than twice as far from the center as the Sun. Clemens' work placed the Sun 8.5 kpc from the galactic center, with a circular rotation speed about the center of 220 km per second. More recent work by Mark Reid and collaborators indicate that the Sun's circular rotation speed is close to 250 km per second. Reid's measurements strongly suggest that the rotation curve of the Milky Way is very similar to that of Andromeda, and so presumably the dark matter components of these two galaxies are also comparable in mass. From Clemens, *The Astrophysical Journal*, (1985): 295, 422.

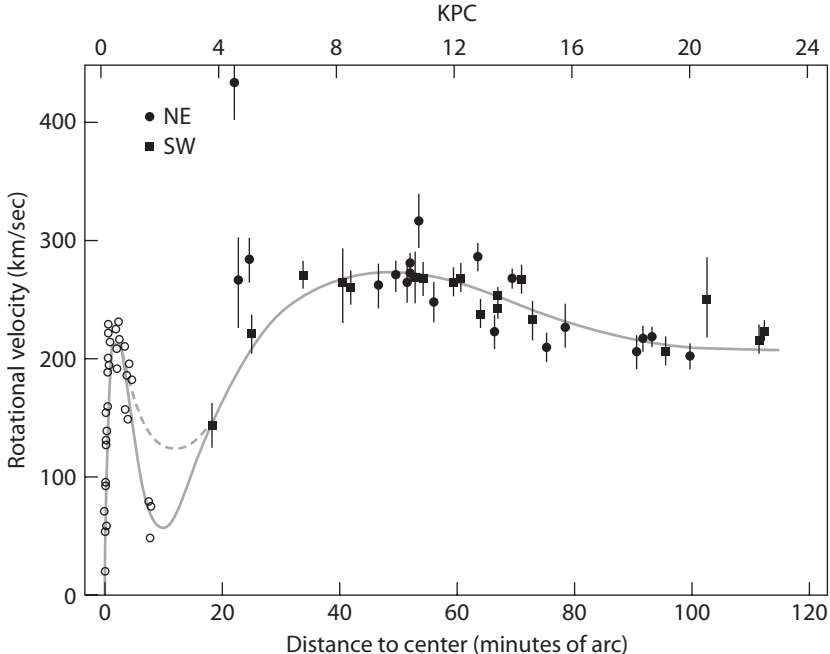


Figure 22.10. Rotation curve for the Andromeda Galaxy, which extends the observed rotational velocities out to 120 minutes of arc, with far more data points than in Babcock's original work. The flat rotation curve continues at least as far out as 7,200 parsecs. From Rubin and Ford, *The Astrophysical Journal* (1970): 159, 379.

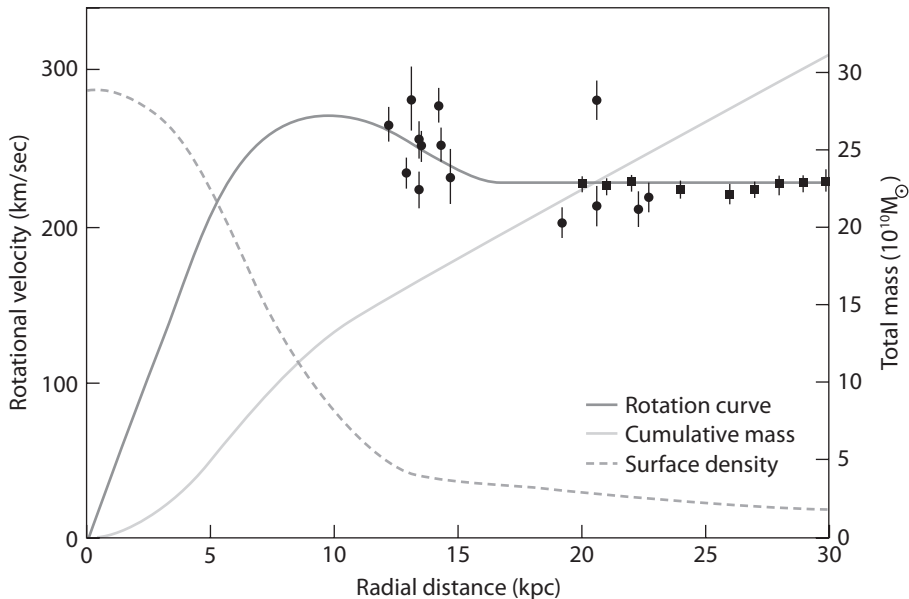


Figure 22.11. Rotation curve (data points with the line drawn through them) for Andromeda that extends the measurements of orbital velocities out to distances of 30,000 parsecs from the center. The line marked “surface density” indicates the amount of mass per square parsec at a given distance from the center. The line marked “cumulative mass” indicates the total mass of the galaxy inside the orbit of a star at a given distance from the center. The flat rotation curve continues at least out to 30 kpc from the center, and the amount of mass climbs steeply from one kpc all the way out to the limits of the data. From Roberts and Whitehurst, *The Astrophysical Journal* (1975): 201, 327.

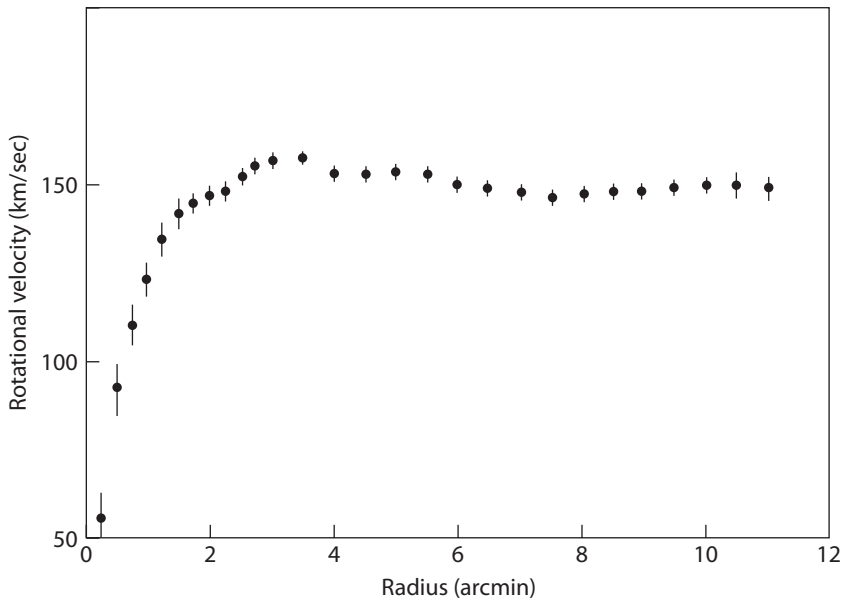


Figure 22.12. Rotation curve for NGC 3198 obtained from radio telescope observations of the orbital velocities of hydrogen gas clouds in this galaxy, showing the flat rotation curve common to galaxies. From Begeman, *Astronomy & Astrophysics* (1989): 223, 47, reproduced with permission © ESO.

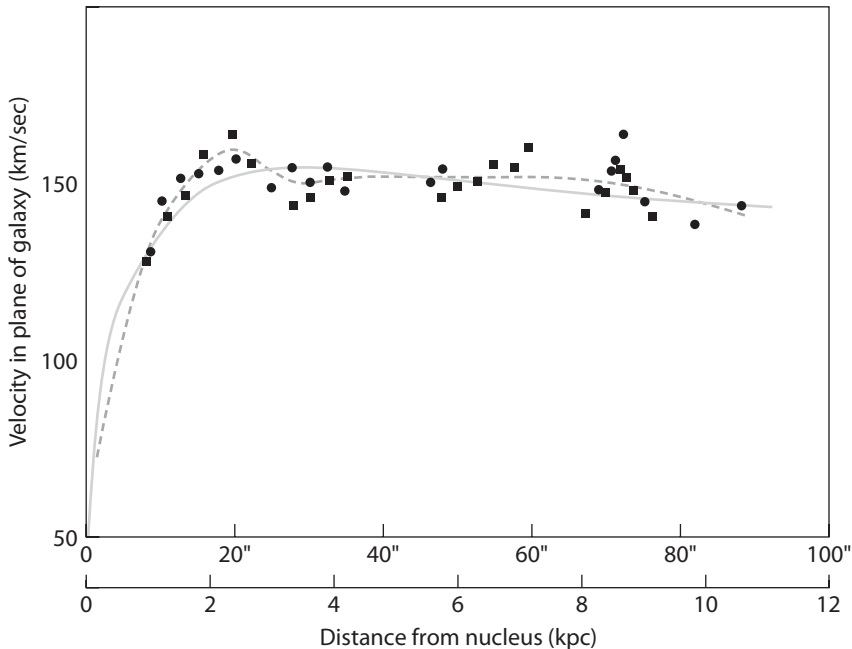


Figure 22.13. Rotation curve for NGC 7217 obtained from visible light observations of orbital velocities of ionized hydrogen gas, showing a nearly flat rotation curve. From Peterson et al., *The Astrophysical Journal* (1978): 226, 770.

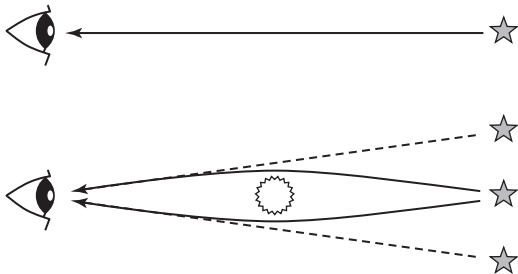


Figure 23.1. Illustration of gravitational lensing. Top, without gravitational lensing, light from a star travels in a straight line to the observer. Bottom, when a large mass lies in between the observer and the star, the observer cannot see the star at the star's true position because of the mass between them. However, light from the star is bent by the gravitational lens, so the observer sees multiple images of the star.

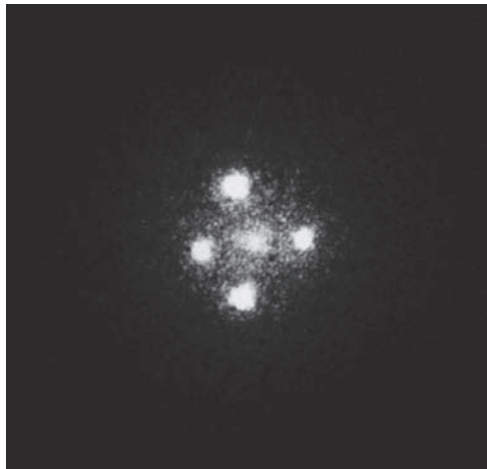


Figure 23.2. The gravitational lensing effect known as Einstein's Cross, in which four images (top, bottom, left, right) of the same distant source are seen lensed by a nearby object (center). In this image, a galaxy only 400 million light years away is lensing a quasar located 8 billion light years away. Image courtesy of NASA, ESA, and STScI.

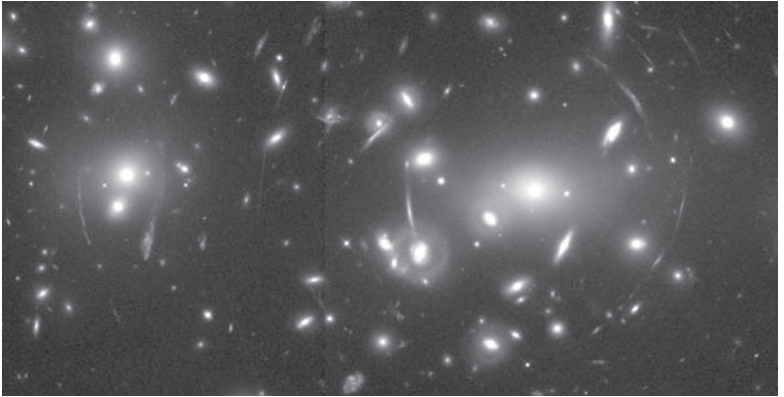


Figure 23.3. Gravitational lensing seen toward the galaxy cluster Abell 2218. The arcs are lensed images of galaxies located five to ten times farther than the lensing cluster. Image courtesy of W. Couch (University of New South Wales), R. Ellis (Cambridge University), and NASA.



Figure 23.4. This composite image shows the galaxy cluster 1E 0657-56, also known as the Bullet Cluster. This cluster was formed by the collision of two large clusters of galaxies, the most energetic event known to have taken place in the universe since the Big Bang. The two large white-gray patches closest to the center show the locations from which X-rays are being emitted from hot gas. The outer two white-gray areas, which overlie the two locations of the visible galaxies, show the locations of the mass responsible for gravitational lensing of more distant galaxies. X-ray image courtesy of NASA/CXC/CfA/M.Markevitch et al. Optical image courtesy of NASA/STScI; Magellan/U.Arizona/D.Clowe et al. Lensing Map courtesy of NASA/STScI; ESO WFI; Magellan/U.Arizona/D.Clowe et al.



Figure 24.1. Left, Belgian priest and physicist Georges Lemaître. Middle, British astrophysicist Arthur Eddington (seated, left), with physicists Henrik Lorentz (seated, right) and Albert Einstein, Paul Ehrenfest, and Willem de Sitter (left to right, standing). Right, Russian-American astrophysicist George Gamow. Photos courtesy AIP Emilio Segrè Visual Archives (center). and The George Washington University Library (right).

Then

Now

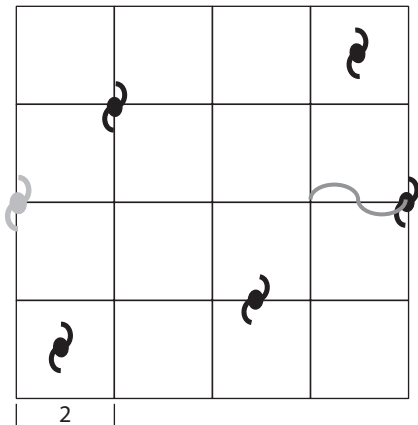
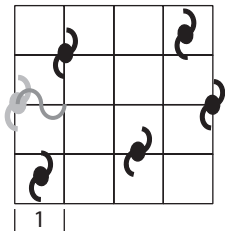


Figure 24.2. Illustration of cosmological redshift: The grid with galaxies represents the universe. On the left, the universe is shown as it was in the past, at a moment when a photon is seen leaving the left-most galaxy. On the right, the universe is seen at the present time, when the photon reaches the right-most galaxy. From “then” until “now,” the entire universe has doubled in size, so that the distances between galaxies are twice as large and the photon itself is twice as large. The galaxies, however, have not moved from their original locations in the universe and have not changed in size.



Figure 24.3. Left, a composite picture, dated 1949, showing Robert Herman (left), Ralph Alpher (right), and George Gamow (center). Gamow is seen as the genie coming out of the bottle of “Ylem,” the initial cosmic mixture of protons, neutrons, and electrons from which, Gamow hypothesized, the elements formed. Right, Robert Dicke. Image courtesy of Princeton University Library (right).

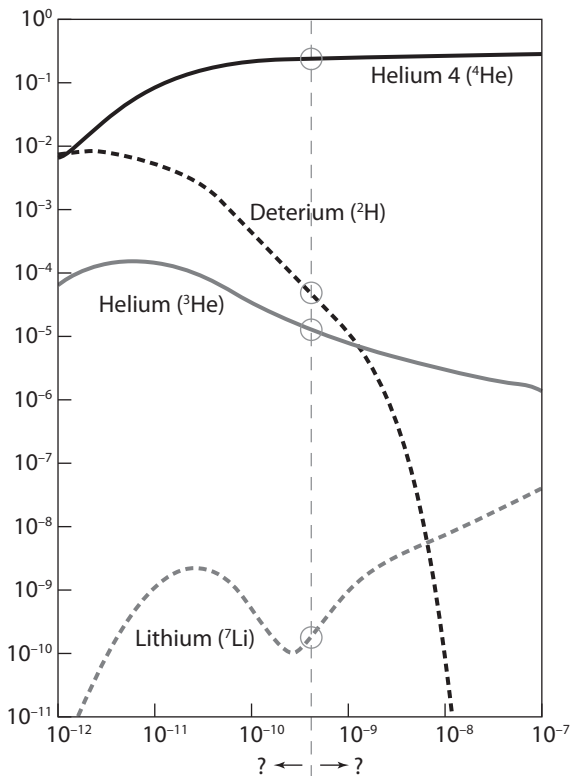


Figure 24.4. The relative amounts of deuterium, helium, and lithium depend on the overall density of normal matter during the first few minutes of the history of the universe, when Big Bang nucleosynthesis took place. For example, if the density were low (left), very little lithium would be produced; if the density were high (right), most of the deuterium and ^3He would fuse into lithium and ^4He . The observed relative amounts (the circles on each curve) of deuterium, helium, and lithium are all consistent with the same density for ordinary matter. Image courtesy of NASA.

TABLE 24.1.
The Early Universe

Age of the Universe	Temperature	Particles	What is Happening
1.5 millionths of a second	1,000 billion K	<ul style="list-style-type: none"> • number of protons and neutrons frozen 	<ul style="list-style-type: none"> • below this temperature, these particles are too massive and can no longer turn back into photons
5 seconds	6 billion K	<ul style="list-style-type: none"> • the number of electrons is frozen • photons cannot travel far before interacting with electrons 	<ul style="list-style-type: none"> • below this temperature, these low mass particles can no longer turn back into photons • the universe is opaque
3 minutes	1 billion K	<ul style="list-style-type: none"> • protons are stable • neutrons decay • there are seven times as many protons as neutrons • all remaining neutrons are stable in deuterium or helium nuclei • 75% of the total mass of all protons and neutrons are in hydrogen, 25% in helium 	<ul style="list-style-type: none"> • protons and neutrons collide to form deuterium nuclei • deuterium nuclei and protons collide to form helium nuclei • nuclear fusion ends
380,000 years	3,000 K	<ul style="list-style-type: none"> • neutral hydrogen atoms • neutral helium atoms 	<ul style="list-style-type: none"> • electrons combine with hydrogen and helium nuclei (recombination) • the universe becomes transparent • CMB is released

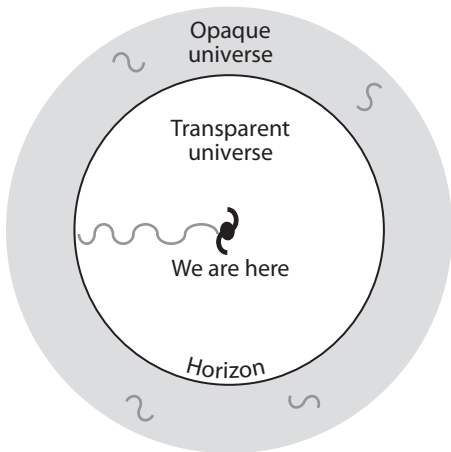
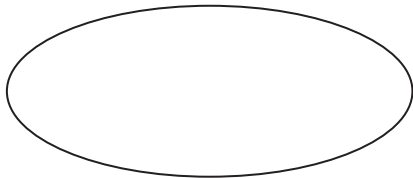


Figure 24.5. The cosmic microwave background consists of photons that were emitted when the universe was about 380,000 years old. In this cartoon, we look outwards from our location in the universe, and when we look outwards we look back in time. Photons emitted about 13.7 billion years ago have been redshifted during their journey toward Earth. Any photons created and emitted in the universe before 13.7 billion years ago cannot penetrate the horizon, as they were absorbed by other particles before they could travel far. On the other hand, at the moment the CMB photons were emitted, the universe was transparent, so those photons have traveled without being stopped or absorbed across 13.7 billion years of time and space to reach our telescopes.



Map of the CMB temperature
of the entire sky: 2.7 K everywhere

Figure 25.1. When viewed from the Earth, the sky appears as a spherical surface that surrounds us. That surface can be presented in the form of a flat map, just as we might produce a flat map of the surface of the Earth. Using more than two decades of measurements of the temperature of the cosmic microwave background, this map presents the temperature of the CMB sky, as measured prior to 1990. Since these observations showed that the CMB had the same temperature everywhere, this map has no structure.

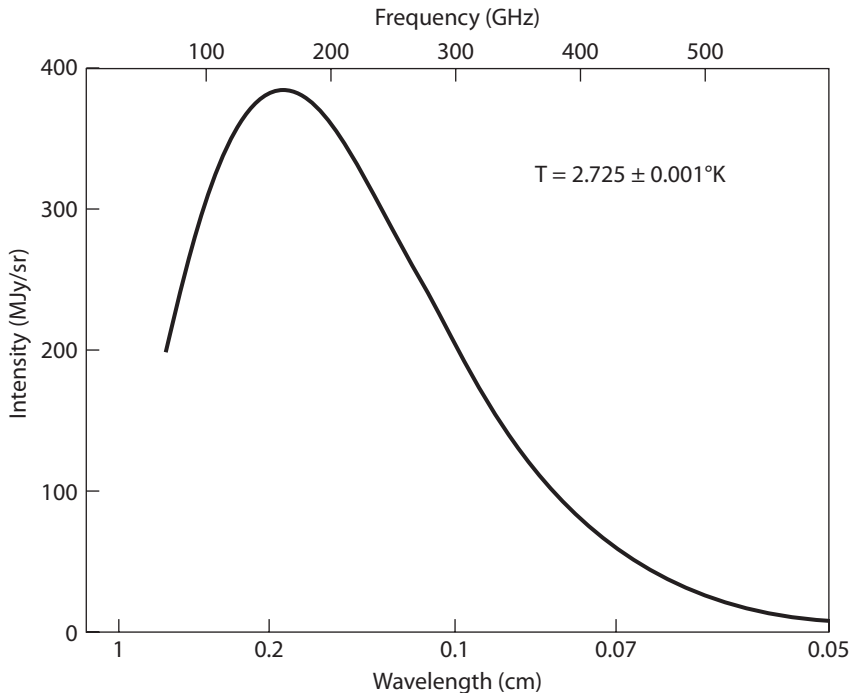


Figure 25.2. Spectrum of the cosmic microwave background obtained with the instrument FIRAS on the COBE satellite. The errors on the thirty-four different measured data points are so small that they cannot be seen under the line drawn for a blackbody with a temperature of 2.725 K. Image courtesy of NASA.



Figure 25.3. World map, showing how the three-dimensional surface of a sphere is depicted as a flat map. The large circle over North America illustrates how a single measurement of the temperature of the Earth, obtained with low spatial resolution, would measure the average temperature over a wide range of latitudes. Such a measurement would not be able to indicate the wide range of actual temperatures. Observations made with higher spatial resolution (small circles) would be able to distinguish the high temperatures in Texas from the much lower temperatures in Canada.

DMR's Two Year CMB Anisotropy Result

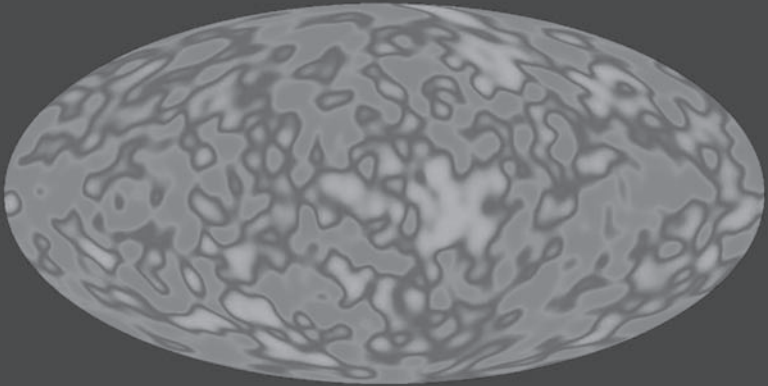


Figure 25.4. Map of the temperature differences in the cosmic microwave background measurements made by COBE. Regions inside black contour lines are as much as 0.0001 K cooler, while gray regions without black contour lines are as much as 0.0001 K warmer than 2.725 K. Image courtesy of NASA.

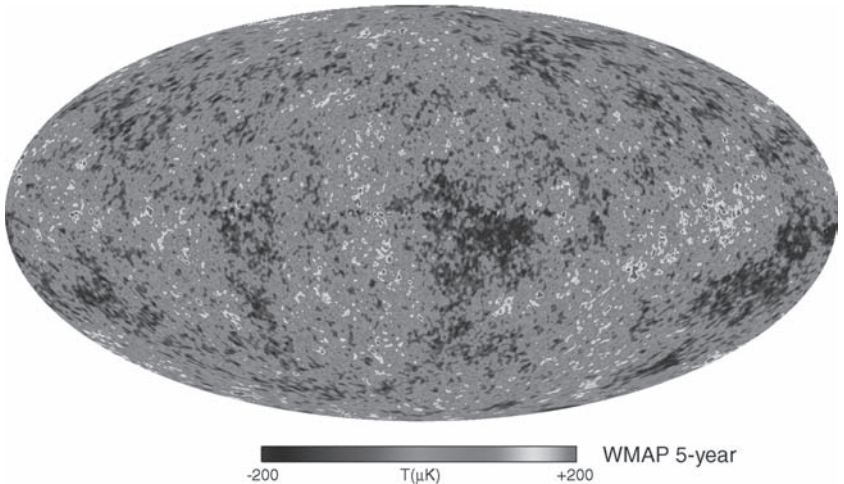


Figure 25.5. Map of temperature differences in the cosmic microwave background measurements made by WMAP. Dark regions are as much as 0.0002 K cooler, while whitest regions are as much as 0.0002 K warmer than 2.725 K. Image courtesy of NASA and the WMAP science team.

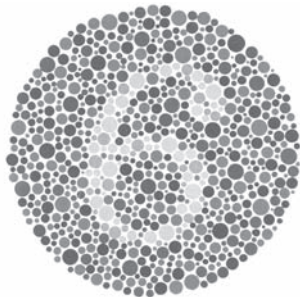
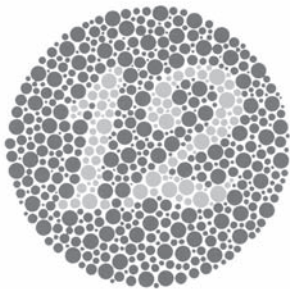


Figure 26.1. Two grayscale versions of Ishihara colorblindness charts. Left, the number “12.” Right, the number “6.” In full-color versions of these charts, colorblind readers would see a random assortment of dots of different sizes and colors in the panel on the right.

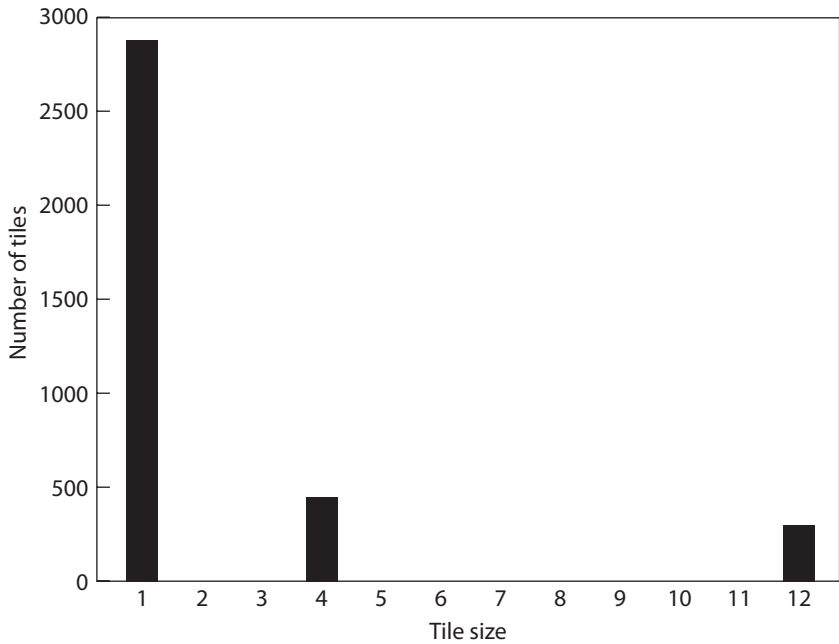


Figure 26.2. Graph showing the number of tiles of each size needed to tile my kitchen: 2,880 1-inch tiles, 450 4-inch tiles, and 300 12-inch tiles.

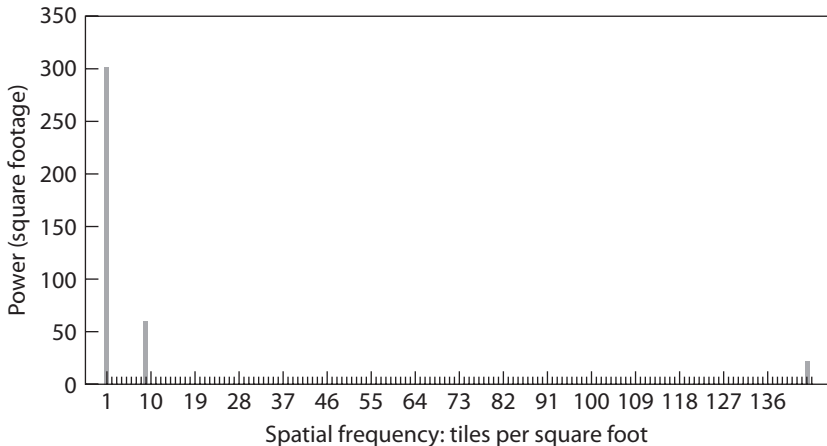


Figure 26.3. Power spectrum for kitchen tiles, in which most of the power (i.e., the square footage covered by tiles of each size) is at low spatial frequencies (big tiles): 300 units of power for the one-tile-per-square-foot tiles, 50 units of power for the nine-tiles-per-square-foot tiles, and 20 units of power for the 144-tiles-per-square-foot tiles.

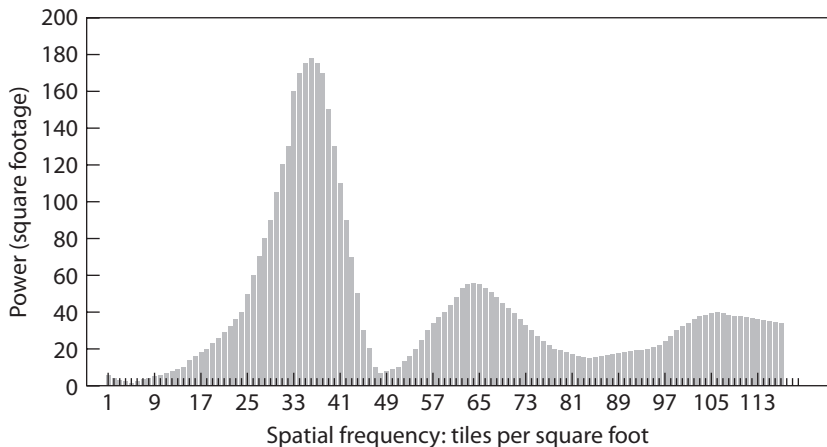


Figure 26.4. Power spectrum for an entire house. In this house, tiles of every size, from one tile per square foot down to more than 100 tiles per square foot, have been used, but larger areas (i.e., power) of the house have been covered in tiles of certain sizes than other sizes. For example, very little power is found in the very largest tiles (one tile per square foot), an increased amount of power is found in intermediate-sized tiles, while the greatest amount of power seen in two-inch-by-two-inch tiles (thirty-six tiles per square foot). This house also has a large amount of power (a secondary peak) in 1.5-by-1.5 inch tiles (sixty-four tiles per square foot).

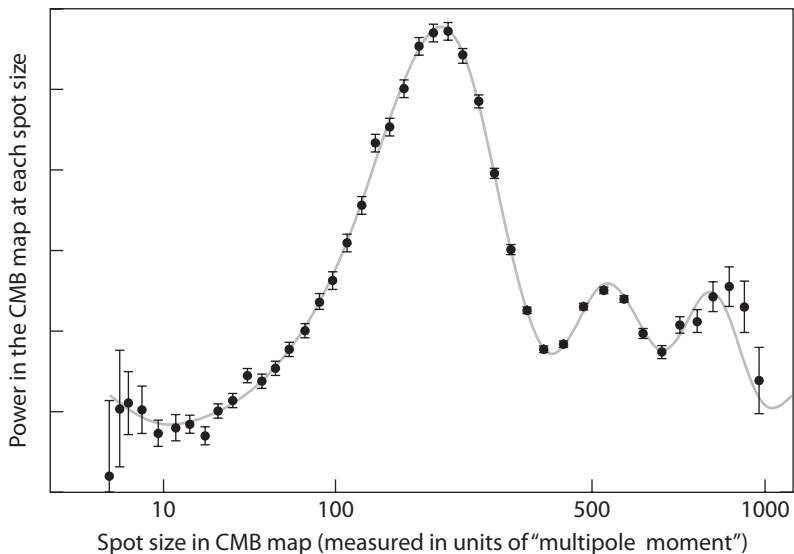


Figure 26.5. The power spectrum of the cosmic background radiation obtained by the WMAP team from five years of data. The values plotted along the horizontal axis are equivalent to spot size in the CMB map, with small multipole moment values corresponding to large (many degrees across) spots and large multipole moment values corresponding to small (fractions of a degree) spots. We can think about the multipole moment as being proportional to the number of spots that could be fitted around the equator of a sphere. The the total amount of power in the map at each spot size is plotted along the vertical axis. The line through the data points is the WMAP team's model fit for a universe with an age of 13.69 billion years. Image courtesy of the WMAP science team.

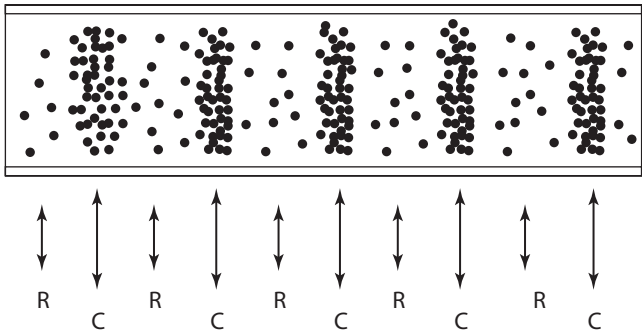


Figure 26.6. A pressure wave in a tube. High-pressure regions (C = compressed) alternate with low-pressure regions (R = rarefied). When the compressed regions expand, they will compress the rarefied gas regions. An initial disturbance at one end of the tube will compress the gas at that end. This disturbance will progress down the tube as a pressure (sound) wave.

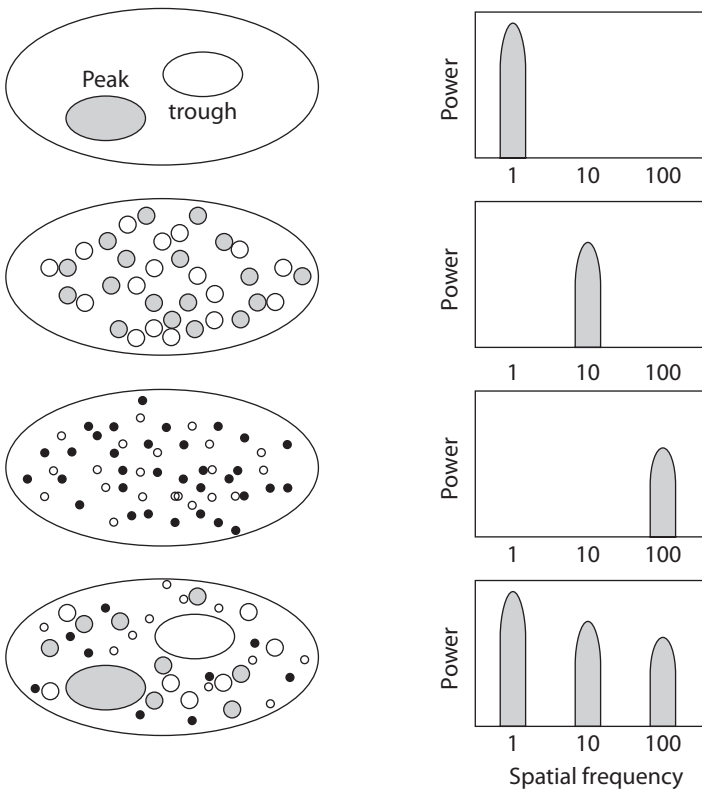
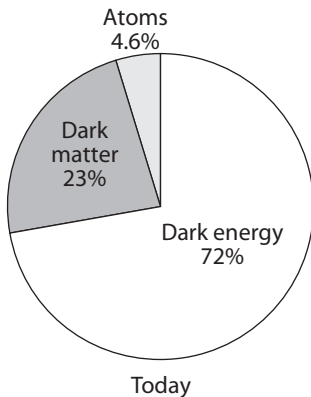
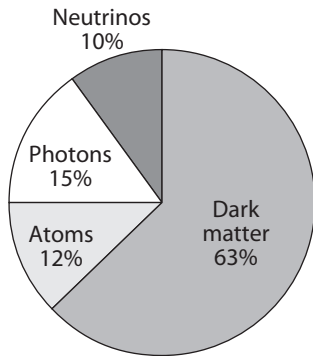


Figure 26.7. Power at different sizes in the map of the CMB. The map of the CMB shows big sound waves (top, left) that appear as peaks (high-temperature regions) and troughs (low-temperature regions) on the CMB map and produce power at a low spatial frequency (top, right). The CMB map also shows intermediate-sized (top-middle, left) and very small-sized (bottom-middle, left) sound waves, each producing power at a unique spatial frequency. The actual map of the CMB is a composite of waves of many different sizes (bottom, left), with a different amount of power at several spatial frequencies, as seen in the power spectrum.



Today



13.7 billion years ago
(Universe 380,000 years old)

Figure 26.8. Pie charts showing the relative proportions of the principle constituents of the universe today (left) and at the moment the CMB photons were released (right). As the universe has expanded, the density of the dark matter (63 percent down to 23 percent) and of the atoms (12 percent down to 4.6 percent) has decreased, since the number of those particles is essentially fixed while the volume of space has increased. Because photons and neutrinos lose energy as the universe expands, the energy densities of these particles decrease faster than the rate at which the matter density decreases. Together, photons and neutrinos contributed 25 percent of the total energy density of the universe 13.7 billion years ago, but today they contribute almost nothing. The dark energy density does not decrease at all, so over time it becomes more and more prominent as the other principle constituents of the universe decrease in energy. Whereas dark energy made virtually no contribution to the total energy density of the universe 13.7 billion years ago, it now dominates the universe. Image courtesy of NASA and the WMAP science team.

TABLE 27.1.
Scientific Measurements for the Age of the Universe

Technique	Derived Age of the Universe
Cooling times for white dwarfs in Milky Way	> 11–13 billion years
Absence of extremely cool, faint white dwarfs	< 15 billion years
Turn off-points for globular star clusters	13–14 billion years
Expansion rate of the universe	13.5–14 billion years
Cosmic background radiation power spectrum analysis	13.5–14 billion years